

Rune Strømholt

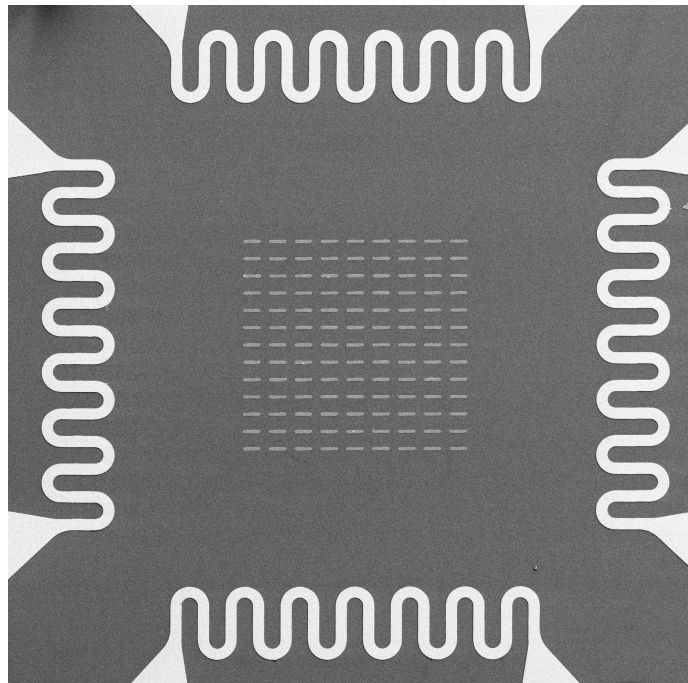
Simulation, design and realisation of on-chip microheaters for artificial spin ice systems

Master's thesis in Nanotechnology

Supervisor: Erik Folven

Co-supervisor: Jakob Vinje

June 2021



Rune Strømholt

Simulation, design and realisation of on-chip microheaters for artificial spin ice systems

Master's thesis in Nanotechnology
Supervisor: Erik Folven
Co-supervisor: Jakob Vinje
June 2021

Norwegian University of Science and Technology
Faculty of Information Technology and Electrical Engineering
Department of Electronic Systems

Abstract

Artificial spin ice (ASI) systems are new and exciting materials within the field of unconventional computing. For this reason, it is necessary to have convenient methods of investigating the structures in different setups, for instance, thermal activation. This thesis aimed to design, simulate and physically realise on-site micro heaters capable of thermally activate spin ice systems. A design consisting of four separate heaters, made up of 150 nm thick copper, each capable of delivering heat individually to the system, was devised, then simulated using COMSOL Multiphysics. Simulations showed the possibility to relatively fast and accurately raise the temperature to about 100 °C, a temperature high enough for this thesis.

Furthermore, a fabrication process using optical photolithography followed by metallisation and lift-off was designed and optimised. In the final process, SPR700-1.0 was chosen as the resist, exposed with a photo dose of 110 mJ/cm² and developed for 40 s using ma-D 332. Furthermore, electron beam evaporation (EBE) was used for metallisation.

To evaluate the capabilities of the heaters, resistive measurements were performed, showing a voltage of 13 V applied to a single heating element could increase the temperature of the system from room temperature to roughly 100 °C. Furthermore, to explore the system in an environment close to its intended use, nanomagnets were fabricated along with the heaters. The systems temperature was lowered to 4 K, and the magnetic properties of the magnets were tested after both heat and magnetic field had been applied to the system. The fabricated heaters were capable of thermally activate the magnets and indicated that it was possible to increase the temperature from a low-temperature system to well above room temperature. Overall the experiment was deemed successful, and the process should be used for further investigations of ASI systems.

Sammendrag

Kunstig spinn-is systemer er nye og spennende materialer innen ukonvensjonell dataprossesering. Det er av den grunn nødvendig å ha lette og praktiske metoder for å undersøke strukturene i forskjellige system, for eksempel ved termisk aktivering. Denne avhandlingen tar sikte på å designe, simulere og fysisk realisere mikroskala varmeelementer som er i stand til å termisk aktivere spin-is systemene. En modell bestående av fire separate varmeelementer, laget av 150 nm tykt kobber, som alle kan levere varme til systemet individuelt eller sammen, ble utviklet og deretter simulert ved hjelp av COMSOL Multiphysics. Simuleringer viste muligheten for relativt raskt og nøyaktig heve temperaturen til omtrent 100 °C, en temperatur høy nok for denne avhandlingen.

Videre ble en fabrikkasjonsprosess med optisk fotolitografi etterfulgt av metallisering og avløftning utviklet og optimalisert. I den endelige prosessen ble SPR700-1.0 valgt som fotoresist, eksponert med en fotodose på 110 mJ/cm² og utviklet i 40 s ved hjelp av ma-D 332.

For å evaluere de termiske egenskapene til varmeelementene ble det utført motstands målinger. De viser at en spenning på 13 V, påført på et enkelt varmeelement, kan øke temperaturen i systemet fra romtemperatur til omtrent 100 °C. I tillegg, for å utforske systemet i et miljø nær det tiltenkte formålet, ble nanomagnetener produsert sammen med varmeelementene. Systemtemperaturen ble senket til 4 K, og de magnetiske egenskapene til magnetene ble evaluert gjennom magnetisk kraftmikroskopi (MFM) både før og etter varme og magnetfelt hadde blitt påført systemet. Målingene viste at varmeelementene var i stand til å aktivere magnetene termisk og indikerte samtidig at det var mulig å øke temperaturen fra et lavtemperatursystem til godt over romtemperatur. Totalt sett ble eksperimentet ansett som vellykket, og prosessen bør brukes til videre undersøkelser av ASI-systemer.

Preface

The following master's thesis has been submitted as a fulfilment for a degree in master of Science from the Norwegian University of Science and Technology (NTNU). It is the final part of a degree in the MTNANO study programme, with a specialisation in nanoelectronics. This thesis is not a continuation of a specialisation project, and all the work has been carried out throughout the spring semester of 2021 under the guidance of Professor Erik Folven at the Department of Electronic Systems, NTNU, and co-supervised by postdoc Jakob Vinje. All the work herein has been conducted by me unless otherwise stated. During the fabrication of nanomagnets, help with the use of the instruments has been given by Anders Strømberg and Jakob Vinje due to limited time and training opportunities for acquiring a licence. Furthermore, Anders Strømberg has helped with the use of the MFM and setting up the system.

I wish to thank all the people whose assistance during my studies has helped me to complete this degree. To name all will take too long, but a couple of people should receive a special thanks.

First and foremost, I would like to thank my incredible helpful supervisors. A huge thanks to my main supervisor Erik Folven, for allowing me to start on something new this spring and finding an incredibly exciting but also challenging project to work on. The weekly meetings have spurred interesting discussions, and it has been a huge pleasure to perform this work for you.

To Jakob Vinje, the incredible wisdom and support you have shown have been a crucial part of finishing my thesis, for which I am incredibly grateful. Having someone with vast experience and knowledge of nano-fabrication to discuss has been a huge help. It has been inspiring to see all the knowledge and humility you carry with you, and you have been both a mentor and friend during this semester.

I would also like to give my deepest gratitude to Anders Strømberg for both helping and training me to use the MFM as well as with the help on the nanomagnet fabrication part.

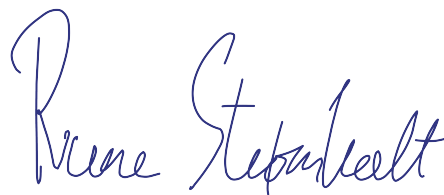
I would like to thank the staff at NanoLab for all the training in all the different instruments used for the fabrication part, as well as the advice they have given

throughout my thesis. Also, a large thanks to Gauarav Sharma for all the help and training in order to master wire bonding.

I would also like to acknowledge The Research Council of Norway for the Norwegian Micro- and Nano-Fabrication Facility, NorFab, project number 245963/F50.

A special thanks go out to my parents for their unconditional support throughout the years, both financially but especially emotionally. They have always only been a phone call away, and I would never have managed to get where I am today without them.

Finally, to my friends and all the people in the amazing student association Timini! Thank you for all the fun and interesting discussion that has occurred at "Timini-kontoret". You have made the last five years an adventure, and my degree would not have been the same without having you around. Furthermore, thank you for all the support along the way, to become "vaffelkonge". I could not have made it without you.

A handwritten signature in blue ink that reads "Rune Strømholt". The signature is written in a cursive style with a large initial 'R'.

Rune Strømholt
Trondheim, June 2021

Acronyms

3DR three dimensional rotator

AFM atomic force microscope

AHA area of interest

ASI artificial spin ice

CAD computer aided design

CVD chemical vapour deposition

EBE electron beam evaporation

EBL electron beam lithography

EUV extreme ultra violet

FEM finite element method

IPA isopropanol

LCC leadless chip carrier

LDPE low-density polyethylene

MFM magnetic force microscopy

NTNU Norwegian University of Science and Technology

PCB printed circuit board

PDE partial differential equations

PVD physical vapour deposition

SEM scanning electron microscope

SLM spatial light modulator

SMU source meter unit

SPM scanning probe microscopy

Contents

Abstract	i
Sammendrag	iii
Preface and acknowledgements	v
Abbreviations	vii
Acronyms	vii
Contents	ix
1 Introduction	1
1.1 Motivation	1
1.2 Project description	2
2 Theory	3
2.1 Joule heating	3
2.2 Heat transfer in solids	4
2.2.1 Conduction	4
2.2.2 Convection	5
2.2.3 Radiation	5
2.3 Magnetism	6
2.4 Artificial spin ice	8
2.4.1 Temperature dependency	8
2.5 COMSOL Multphysics	10
2.6 Characterisation techniques	11
2.6.1 Optical microscopy	11
2.6.2 Scanning electron microscopy	12
2.6.3 Magnetic force microscopy	12
2.7 Photolithography	14
2.7.1 Chemicals	14

2.7.2	Process flow	15
2.7.3	Metallisation and lift-off	17
2.8	Electron beam lithography	17
2.9	Electron Beam Evaporation	18
2.10	Wire bonding	19
3	Experimental	21
3.1	COMSOL simulations	21
3.2	Realisation of the proposed design	22
3.2.1	Photolithography - dose and development testing	23
3.2.2	Physical realisation of micro heaters	25
3.2.3	Fabrication of micromagnets	26
3.2.4	Fabrication of nanomagnets	26
3.2.5	Characterisation of the fabricated structures	27
3.2.6	Scribing and wirebonding	27
3.3	Characterization of heating	27
3.3.1	Magnetic measurements	28
4	Results	31
4.1	COMSOL Simulations	31
4.2	Physical realisation of the system	38
4.2.1	Using optimised lithographic process for fabricating microheaters	43
4.2.2	Fabrication of micromagnets using optical lithography and metallisation	45
4.2.3	Fabrication of nanomagnets using electron beam lithography and metallisation	46
4.3	Characterisation of thermal properties of heater	48
4.3.1	Thermal measurements of the heater	48
4.3.2	Magnetic force microscopy measurements of the nanomagnets	50
5	Discussion	59
5.1	Simulations	59
5.2	Fabrication process	60
5.3	Thermal characterisation	62
5.3.1	Heating properties	62
5.3.2	MFM measurements	63
6	Conclusion	67
6.1	Further Work	68
	References	69
	Appendices	72

A Simulation of micromagnet	72
B Simulation of single heater	73

1 | Introduction

1.1 Motivation

Over the last couple of decades, no technology has had a more significant impact on society than computers, and humanity is becoming increasingly more dependent on having easy access to computing devices. Not only does the average person have a need for better computers, but the increased demand for more computing power in groundbreaking research such as development for new vaccines, simulation of complex materials and artificial intelligence makes it crucial to further improve on today's computers. Now, as Moore's law is coming to a halt [1], it is necessary to discover novel ways of improving on today's computers by thinking new. The field of unconventional computing [2].

One such area of unconventional computing is using artificial spin ice (ASI) to create self-organised structures that can work as a system for data analysis. Jensen et al. showed in 2018 the possibility of using ASI as a "substrate for material computation" through micromagnetic simulations. By arranging nanomagnets in a specific orientation and applying magnetic fields of different strengths and frequencies, the system allows for unique states. These states could then be used to work both in a one-to-one and many-to-one input-output manner, allowing for memory storage [3]. Moreover, Hon et al. showed in 2021 the possibility of using ASI for reservoir computing (RC) [4], which is a good candidate for neuromorphic computation. The idea of fabricating computers and devices inspired by the brain [5].

As unconventional computing using ASI is still in its infancy, it is essential to establish suitable research methods to improve on the field. One particular method of interest is the ability to heat the systems accurately, locally, and fast [6]. Therefore, this project will focus on fabricating an on-chip micro-scale heater, using resistive heating to increase the temperature of the spin ice structures relatively fast and locally. Furthermore, establishing protocols for fabricating on-chip microheaters can not only help research within the field of ASI, but also in other areas where fast and local heating is needed, such as biological research [7] or even in lithography processes [8].

1.2 Project description

At the beginning of this project, three properties were defined as to how the heater should work. The properties are based on empirical observations on studies of the magnets within the research group. The properties are as follows:

1. The device should be able to heat an area of roughly $200 \times 200 \mu\text{m}$ to an even temperature of approximately $100 \text{ }^\circ\text{C}$. This is the area the ASI-structures is deposited and are hereafter called the area of interest (AHA).
2. The heating should be relatively quick, roughly within a second or two, and stabilise at the desired temperature.
3. The final design should allow for the creation of a temperature gradient across the AHA.

Thereafter, the project was divided into three main parts. Firstly, simulations using COMSOL Multiphysics was performed in order to arrive at a design that could achieve the three properties defined above.

Secondly, fabrication using photolithography along with metalisation took place. A considerable part of this project was to arrive at an easy, replicable and accurate fabrication process in order for the heaters to be used in further research. Therefore different aspects of the fabrication process, especially during the photolithography part, was tested to arrive at the best process. Furthermore, both $\text{Ni}_{0.8}\text{Fe}_{0.2}$ micro- and nanomagnets, was fabricated to examine how they would react to temperature from the heaters.

In the end, the thermal properties of the fabricated design were evaluated. The temperature was measured using resistive measurements on the heaters. Thereafter, magnetic force microscopy (MFM) was used to evaluate the thermal response of nanomagnets to establish if the heating elements work for their intended purpose.

To summarise, this project aims to fabricate micro heaters that can be added fabricated directly on the wafers carrying the artificial spin ice structure in a convenient, fast and easy way. The goal of the thesis will be to establish protocols for a versatile and convenient fabrication process.

2 | Theory

Throughout this chapter, the relevant theoretical background needed to understand and discuss the results of this thesis will be presented. To start with, the theory behind heat generation from electrical currents, as well as heat transfer in solids, is explained. Thereafter, magnetism and how it depends on temperature is presented before moving on to the concepts needed for simulating, fabricating and characterising the device.

2.1 Joule heating

Joule heating, or Ohmic- or resistive heating, is the concept of generating heat using electric currents. First discovered by James Prescott Joule in 1840 [9] as well as independently studied by Emil Lenz, culminating in Joules-Lenz law. The law states that the power, P , generated by the current through a material is given as,

$$P = RI^2, \quad (2.1)$$

where R is the resistance, and I is the current through the material. The power will generate heat within the conductor. Combining this with the fact that the resistance R is inverse proportional to the area A of the conductor,

$$R = \frac{\rho L}{A}, \quad (2.2)$$

one can conclude that thinner conductors will have a higher resistance and hence a higher power [10]. Here ρ is the material's resistivity and L length conductor. The heat generated can be explained by collisions between the travelling electrons and the lattice of the conductor. The energy of the electrons will transfer to the lattice during collisions which cause the lattice to vibrate, generating phonons and heating the material [11].

The resistivity ρ of a conductor is a material property that indicates the electrons ability to travel through the material. This value is not only dependent on the type of material but also the temperature. The equation,

$$\rho(T) = \rho_0(1 + \alpha(T - T_0)) \quad (2.3)$$

shows how the resistivity of a metallic material increases when the temperature increases. Here α is the temperature coefficient of resistivity, T_0 is the start temperature, T is the temperature of the material, and ρ and ρ_0 are the end and start resistivities [10]. This effect can be explained at an atomic level as it will be harder for electrons to move through the material due to a higher chance of colliding with the lattice, or more accurately, the phonons. When the temperature increases, there are more phonons from which the electrons can collide and scatter.

Important to note is that this temperature dependency is only linear within certain intervals, as the temperature coefficient of resistivity α changes at different temperatures. At room temperature, α for copper is 0.00393 while 0.00431 for aluminium [12], indicating that the resistivity increases with 0.393 % and 0.431 % for each degree increase. At low temperature, impurities in the crystalline structures begin to limit the resistivity of the metal, and therefore, the temperature dependency decreases. This happens at roughly below 100 K [13].

2.2 Heat transfer in solids

The first law of thermodynamics states that energy cannot be created or destroyed, only transported from one place to another,

$$\delta U = Q + W. \tag{2.4}$$

In other terms: "The change of internal energy for a closed system, δU is equal to the heat supplied to the system, Q , minus the work done by the system W " [14].

Thus, energy transport within a system will happen by either the movement of heat between parts of the system or by work performed within the system. The temperature of a system is directly related to its internal energy, and therefore to determine the change in temperature, determining how the internal energy change is necessary. For incompressible, solid objects that do not change in volume, heat is the only means of energy transport [14]. There are three primary forms of heat transfer. These are convection, conduction and radiation and are summarised in the following.

2.2.1 Conduction

Conduction is the transfer of heat within or between bodies due to collisions between particles such as molecules, atoms and electrons on the microscopic level. This causes the transfer of kinetic and potential energy between the particles. Fourier's law describes the heat flux from a body,

$$\mathbf{q} = -\kappa \nabla T, \tag{2.5}$$

which says that the heat flux density is proportional to the thermal conductivity κ and the negative temperature gradient at a given point. This can easier be described by the heat flow through a given area as shown in,

$$\frac{Q}{\delta t} = -\kappa A \frac{\delta T}{\delta x}. \quad (2.6)$$

The thermal constant κ is different for different materials and indicates how easy the flow of heat is within a material. A good electrical conductor such as copper often also works as a good thermal conductor having a $\kappa = 385.0 \text{ W/mK}$ due to the free electrons helping with heat transport [14]. Semiconductors often have a bit lower conductivity than metals. Silicon for instance have a $\kappa = 169 \text{ W/mK}$ [15] at room temperature, but the value is highly dependent on the temperature and reaches as high as $\kappa = 2800 \text{ W/mK}$ at 30 K [16]. Insulators, on the other hand, such as low-density polyethylene (LDPE) have very low conductivity with $\kappa = 0.33 \text{ W/mK}$.

2.2.2 Convection

Convection is a form of heat transfer that occurs in fluids. It is a form of transfer that happens due to the movement of particles within the fluid, moving heat from one place to another. Natural convection arises due to air being heated from a heat source resulting in a less dense fluid, which again will rise due to buoyant forces. Colder and denser air will then take the place of the hot air, which can again be heated. The convective heat flux can be described by the equation,

$$q = h(T_{ext} - T), \quad (2.7)$$

where h is called the heat transfer coefficient [14]. The heat transfer coefficient is a complex quantity as it is dependent on several parameters, but it has been measured for given situations. For instance, natural convection between a solid and air has been measured to roughly $5 \text{ W/m}^2\text{K}$ to $55 \text{ W/m}^2\text{K}$ [17].

2.2.3 Radiation

Convection and conduction is heat transport on the molecular level by moving particles through a physical medium. Radiation, on the other hand, is energy transport by photons, which does not require a medium. When charged particles accelerate, they will induce radiation, and within a hot object, particles both charged and uncharged will vibrate and collide. Generating photons The net heat flow of the system due to radiation follows Stefan-Boltzmann law,

$$\frac{Q}{t} = \sigma(T_2^4 - T_1^4)A, \quad (2.8)$$

where σ is Stefan-Boltzman constant A is the surface area, and T_2 is the temperature of the object while T_1 is the temperature of the surroundings. The emissivity e is a material-dependent constant between 0 and 1 and indicates how good the radiation of the object is. This constant is very dependent on the material, both the colour and composition and can change with different temperatures [14].

2.3 Magnetism

Magnetism is one of the fundamental interactions in nature and can be understood both from magnetic fields given by electric currents or from the inherent magnetic moments of elemental particles. Protons, neutrons and electrons, all having an intrinsic property called spin which carries with them a magnetic moment μ given by the equation,

$$g\frac{q}{2m}\mathbf{S}. \quad (2.9)$$

Here, g is a particle dependent factor called the g-factor, while m and q are respectively the mass and charge of the particle. \mathbf{S} is the spin angular moment of the particle and specify if the spin is in a spin-up state or a spin-down state.

Some atoms contain unpaired electrons, providing the atom with a non-zero magnetic moment and a net spin. When these are subjected to an external electric field, the electrons align themselves with the field, further enhancing it. These materials are called paramagnetic, and an illustration of these are given in figure 2.1. While the external field is on, the total magnetic field of the system is the sum of both the external and internal field. However, as the spins prefer to orient in different directions to minimise energy, the magnetic moment relaxes back to the ground state when the field is turned off again.

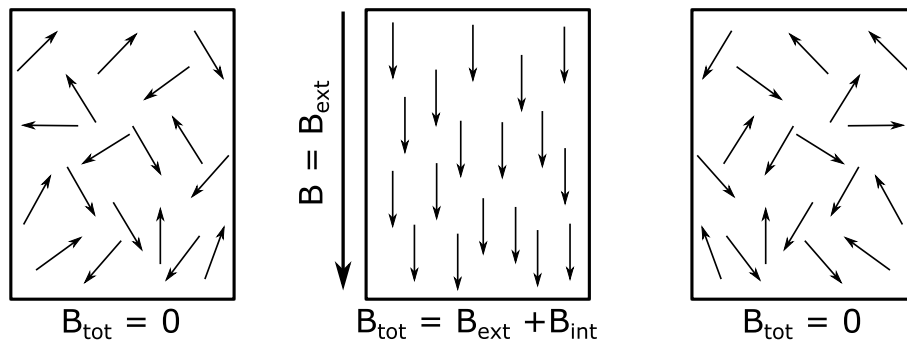


Figure 2.1: Illustration of how paramagnets work. Before any magnetic field is applied, the spin will arrange in a random manner. As an external magnetic field b_{ext} is applied, all magnets will align with the field, and the total field of the system, B_{tot} , is the sum of the external field and the total contribution of all spins in the material B_{int} . After the external field is switched off, the spins will arrange in a random manner again, resulting in zero magnetisation.

In ferromagnets, on the other hand, the spins prefer to orient themselves in the same direction. This is due to the exchange interaction where electrostatic interactions dominate. For these materials, spins are further apart when they point in the same direction, providing the system with lower electrostatic energies. The system will, therefore, minimise its internal energy when the spins align. However, for bulk systems, the total energy landscaped will not accommodate all spins pointing in one direction. In this case, magnetic domains are created. An illustration of this is given in 2.2(a). The total system consists of several domains separated by a domain wall, where within each domain, all the spins points in the same direction. Before any external field is applied, each domain will then align in directions that minimise the entire energy landscape. On the other hand, when a magnetic field is applied, the domains align, and most will stay aligned after the external field is switched off.

The creation of these domain walls demands a certain amount of energy, and for small magnets where the total internal energy is low, this energy is too high for the walls to form. As such, single domain magnets are created. An illustration of a single domain magnet is shown in figure 2.2(b). Here, all spins within the magnet points in the same direction, as indicated by the arrows in the illustration. This is often the case for magnets on the sub-micrometre scale [18].

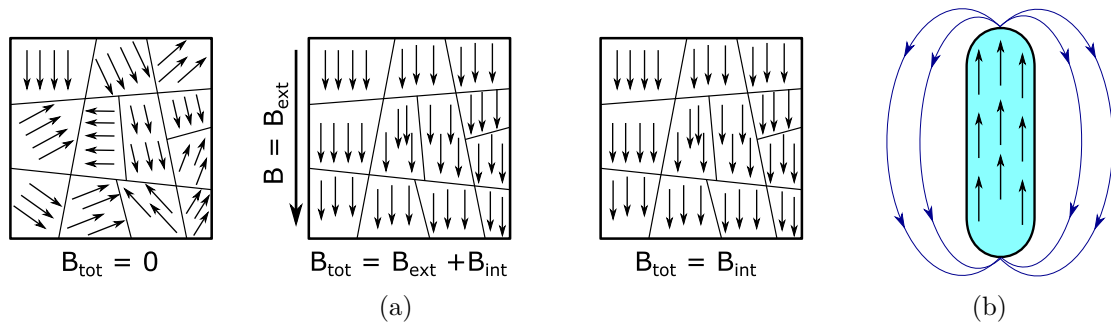


Figure 2.2: **a)** Illustration of how ferromagnets work. The magnet contain, several domain where in each domain, all spins are pointing in the same direction. However, the total magnetization of the system is zero, as all domains will arrange in a random directions. As an external magnetic field b_{ext} is applied, all domains will will align with the field, resulting in a field $B_{tot} = B_{ext} + B_{int}$ where B_{int} is field contribution of the internal domains After the external field is switched of, the domains will prefer to maintain the direction, resulting in net magnetisation. **b)** An illustration of an elongated single domain ferromagnet, along with the field lines. As the formation of a domain wall is to energy-intensive, all spins align in the same direction. Furthermore, due to the high aspect ratio of the magnet, it can only hold to magnetisation. either up or down.

2.4 Artificial spin ice

Artificial spin ice (ASI) systems were first developed in 2006 by Wang et al. [17], using an array of single domain ferromagnets to mimic the spin-ice formations found in pyrochlore structures in nature. The name "spin-ice" arises from how the hydrogen atoms arrange in ice, where they exist in frustrated states. The entire energy landscape does not allow for minimising each interaction in the system. Thus lowering the temperature to absolute zero will not give zero entropy. The same type of frustration is observed in other structures as well such as the magnetic moments in $\text{Ho}_2\text{Ti}_2\text{O}_7$ and $\text{Dy}_2\text{Ti}_2\text{O}_7$ [19].

Today, artificial spin ice structures consist of elongated single domain nano-magnets arranged in specific patterns that create frustrated states within the system. Such arrays can be seen in figure 2.3(a). The illustration shows the ground state of both a square lattice formation and a kagome lattice formation. As one can observe, magnets of the same orientation are pointing towards each other, indicating frustration. Figure 2.3(b) show the different configurations the spins may have, with increasing energy from left to right, for both lattice formations. The ring indicates the flux closure of the magnets, which, if type 2,3 or 4 for the square lattice, or type 2 for the kagome lattice, is added to the system, will break. This can then lead to what is known as emergent monopoles, an interesting phenomenon of these systems that can be used for computation [6].

2.4.1 Temperature dependency

The magnetic properties of ferromagnets are dependent on the temperature of the system. As the temperature of the system increases, the effect of the exchange interaction is reduced, and at a temperature called the Curie-temperature, the ferromagnets switch towards paramagnets. One measurement of the magnetic properties of a material is the magnetic susceptibility χ . The magnetic susceptibility for ferromagnets relates to the temperature as given in,

$$\chi = \frac{C}{T - T_c}, \quad (2.10)$$

where C is a constant called the Curie constant, and T and T_c are the system temperature and Curie-Temperature, respectively.

Furthermore, the elongated single domain ferromagnets within the ASI have their own curie temperature, also called the ordering temperature. As explained, for ferromagnet, the temperature of the system reduces the effect of the electrostatic interaction of the spins. This effect also exists on the macro-scale, where the magnetostatic interaction between each magnet is reduced compared to the energy of the system, and at a given temperature, their system becomes disordered. The

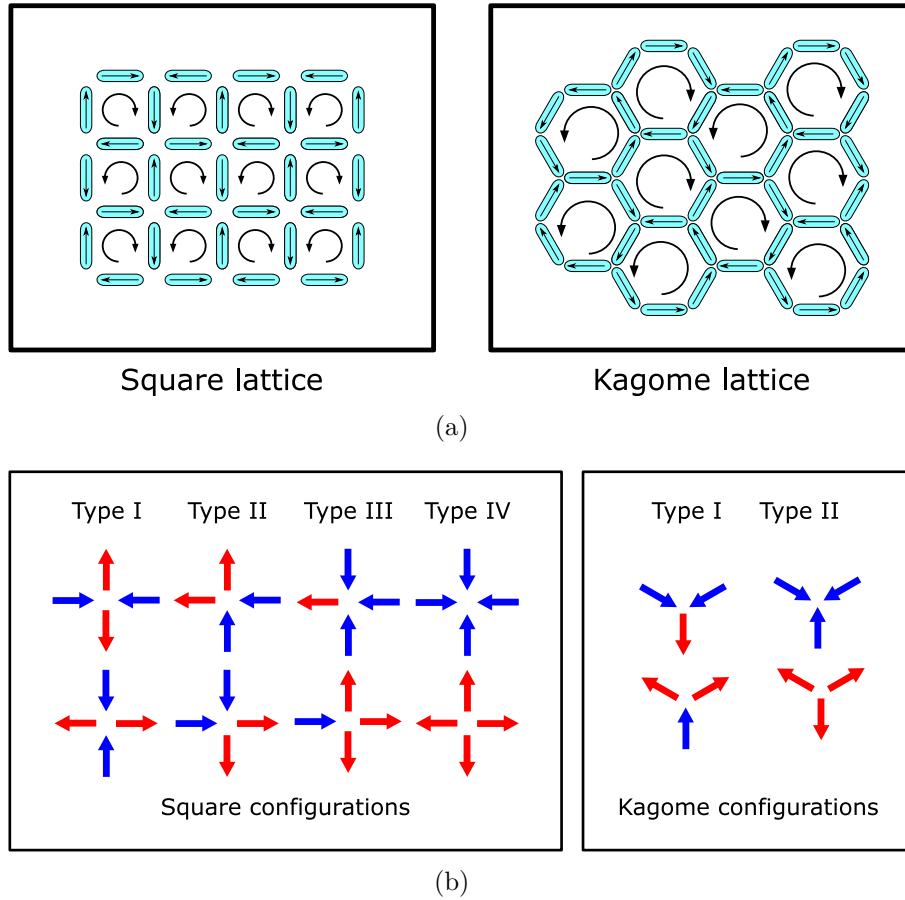


Figure 2.3: Illustration of how elongated single domain ferromagnets can be arranged to create artificial spin ice systems. **a)** Illustrates two different artificial spin ice systems. The Square lattice formation, and Kagome lattice formation. **b)** Shows some of the different magnetic moment configurations for both square lattice and kagome lattice, with increasing energy from left to right. Square lattice Type II and Type III have three and seven, respectively more configurations of equal energy that are not shown.

ordering temperature of the magnets occurs at a lower temperature than the Curie-temperature [20].

One interesting property with elongated single domain ferromagnets is its ability to "withstand" an external applied magnetic field. From figure 2.4 an illustration of a hysteresis curve for ferromagnetic is given. If a magnet is initialised with a magnetisation of M_s , it will remain in that magnetisation until a field strong enough manages to flip it. This field is called the coercive field H_c . Coercivity is the magnets ability to withstand this external magnetic field, and this decreases with temperature. Therefore, the magnets can switch with a low external field if the temperature is high enough. The temperature dependency is highly dependent on the size of the magnet [21].

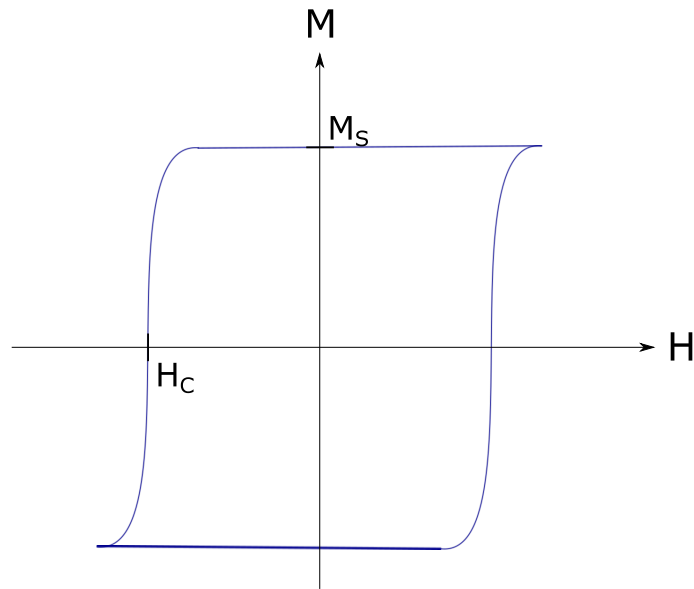


Figure 2.4: Hysteresis curve for an elongated single domain ferromagnet. After the magnet has been saturated giving it a magnetisation of M_S , a magnetic field of H_C , called the coercive field, is required before the magnetisation flips.

2.5 COMSOL Multiphysics

COMSOL multiphysics is a software platform design to simulate physic-based problems. It combines different physical phenomena into one problem solving this now coupled system [22]. Most physical problems today can be described using partial differential equations (PDE)s, which necessarily cannot be solved using analytical calculations, and a numerical approach is necessary. COMSOL uses the finite element method (FEM) in order to solve the PDE which discretises the problem from a continuous equation to a set of linear equations possible to solve numerically. In FEM calculations, the domain of interest is divided into a set of elements called the mesh. Each element is then connected to the linear equations and the boundary conditions. This gives a finite number of linear equations that can be solved numerically by the computer. Finer meshing results in more elements, which could give more accurate solutions, but also demands more time, memory and computing power in order to converge [23, 24]

There are three main parts of stimulating in COMSOL. First, the type of problem has to be defined. That is, what physical aspects, or equations, should be calculated during simulations. Here, it is essential to only add relevant physic problems as the more equations the system has to solve, the longer time it takes. For instance, If the system's current is of interest, adding heat distribution could be relevant, as resistivity changes with temperature. Adding induced magnetisation, on the other hand, might be excessive unless the system consists of spools or large currents. The

built-in multiphysics model will then combine the solutions of these equations during simulation in order for them to interact.

The second part is defining the geometry and mesh of the system. The geometry can be imported as a computer aided design (CAD) file from other software, but it is also possible to use the built-in geometry compiler. Using this compiler can be beneficial if parameterisation of the structure is desired, as one can perform parametric sweeps using variables defined during compilation. Having a proper understanding of the system is also instrumental in optimising the simulations. If a general understanding of the evolution of the system is known, one can limit the accuracy of the mesh in a direction recognised the system would not change substantially or evolve linearly. For instance, having large areas where heat distribution occurs will most likely not need very fine meshing unless obstacles or other elements can affect the heat flow [25].

The third part is defining the study and performing the simulations. Several studies can be performed, such as standard stationary studies, time-evolution studies and otherwise. In this step, the solver configuration is also selected, which tells the system how the equations should be calculated—, for instance, using a segregated or fully coupled solver, where for each iteration, the equations are either solved in separate steps then combined, or at the same time. The last will require much more memory but might be faster and more accurate. COMSOL chooses a default solver configuration that should be work for the physic modules chosen. Nevertheless, the geometry and materials of the system are not considered in the default solver, and it might be necessary to optimise the configuration for the problem at hand [26].

2.6 Characterisation techniques

2.6.1 Optical microscopy

An optical microscope, or light optical microscope, is a characterisation tool that uses visible light to observe images of small samples. Basic microscopes use a system of lenses, magnifying the image of the sample that, in turn, can be viewed by the user. Either by using an eyepiece or generate digital images that can be viewed instantly at a computer screen [27].

There are several different types of microscopes, each with its advantages and disadvantages. One type of microscope that can, for instance, be used in a lithography process is a bright-field microscope. Light is radiated on the sample, which in turn is reflected through the lenses towards the user. Different lenses give different magnification, and by adjusting the height of the sample, one can adjust the focus by allowing the focal plane to coincide with the sample. Ernst Abbe's diffraction

limit gives one important limitation of bright-field optical microscopes,

$$d = \frac{\lambda}{2NA}. \quad (2.11)$$

Here d is the smallest feature size possible to observe, λ is the wavelength of the light, and NA is the numerical aperture, which indicates how good the lenses are. Therefore, magnification is limited by the wavelength of the light used, and it is challenging to observe features in the x-y plane of less than one-micrometre [28]. Despite this, the wavelength of light reflected by the sample can depend highly on the thickness of the material inspected, and therefore it can be possible to differentiate the thickness of parts in the sample on the low nanometre scale.

2.6.2 Scanning electron microscopy

Scanning electron microscope (SEM) is a widely used imaging technique used to observe structures on the micro- and nanometer scale. It utilises a focused beam of electrons to scan a surface. When the electrons approach the surface, they will scatter and release electrons from the surface, which are subsequently picked up by a detector. The topology of the sample will change how the sample electrons are scattered, and by measuring the intensity of electrons in each point, one can generate an image of the sample. During the scanning, electrons are focused using electrostatic lenses that push the electrons towards the centre. As opposed to optical microscopes, where the wavelength of light limits the resolution, the resolution in an SEM is limited by aberrations in lenses. That is, the ability to focus the electrons towards a centre.

Furthermore, as the sample is bombarded with electrons, a build-up of charge on the sample's surface can occur if the sample is not conducting enough. This can deflect the electrons and disturb the imaging. This can, for instance, be a problem when inspecting samples such as photoresist. A solution to overcome the charging is to coat the sample with thin layers of conducting materials, or if the sample allows for it, use conductive tape on top of the sample close to where inspecting. Moreover, SEM also needs to be held under a high vacuum, as the electrons can be disturbed by other particles in the air, which in turn limits the type of samples that can be used in the SEM [29].

2.6.3 Magnetic force microscopy

Magnetic force microscopy (MFM) is a scanning probe microscopy (SPM) technique that uses a magnetic tip in order to evaluate stray magnetic field lines of a sample. The working principles of an MFM are very similar to an atomic force microscope (AFM); in fact, the MFMs can be used as an AFM as well. Figure 2.5 shows a simplified cartoon of the working principles of an MFM, where a cantilever carrying

a magnetic tip is transported along the sample in order to assess the magnetic field lines from the sample.

There are several modes of imaging that can be used when working with MFMs and AFMs; one such mode is tapping mode. The tip is applied a periodic tapping motion, given by a sinusoidal function. In contact mode, the MFM works as an AFM, and the tip is in contact with the sample where van der Waals forces are dominant. As the height of the sample changes, the height of the cantilever changes, deflecting a laser light cast on the spring. By measuring the deflection angle, it is possible to determine how much the cantilever has lifted. In MFM mode, the tip is lifted above the sample, where the tip is more sensitive to magnetic fields than Van der Waals forces. Due to the cantilever acting as a spring, the periodic motion of the tip is phase shifted from the applied periodic motion. When the tip is affected by a magnetic field, this phase will change, which can be detected by the laser. The strength and direction of this shift can then again be mapped into an image of the magnetic lines [30, 31].

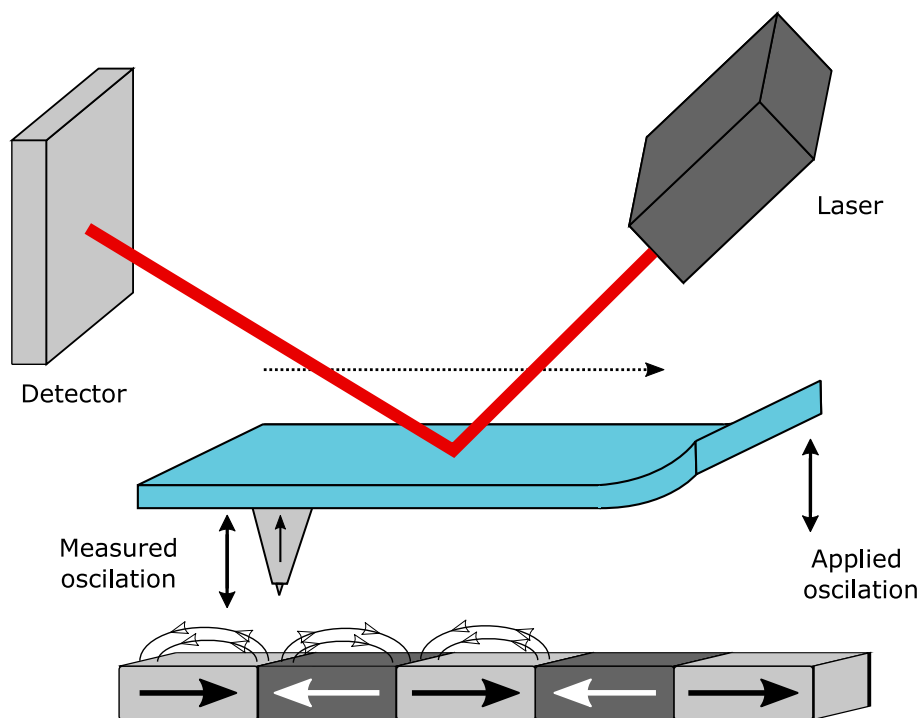


Figure 2.5: A simplified cartoon showing how an MFM works. A cantilever carrying a magnetic tip as scanned across the sample, while a sinusoidal motion is applied. The magnetic field lines of the sample will deflect the cantilever, causing a phase shift motion of the cantilever, which is measured by the laser.

2.7 Photolithography

Photolithography, or optical lithography, is the most used technique for manufacturing integrated circuits and fabricates patterns with dimensions on the nano- and micrometre scale. It is a process that is based on standard lithography, originally used to print music sheets, and has the possibility of mass fabricating a specific pattern [32]. Optical lithography uses UV-light to change the solubility of a resist on a given substrate, thereby leaving a specific pattern within the resist. Wavelengths of the light used in this process ranges from 400 nm all the way down to extreme ultra violet (EUV) light of 13 nm [33]. Although, using wavelengths on the EUV level, demands large scale and expensive equipment, therefore in normal lab environments UV light of 405 nm(h-line) and 365 nm(i-line) is often used. Techniques such as metallisation and etching can then be used in order to leave a lasting pattern of the desired material on the sample [34].

2.7.1 Chemicals

Several chemicals are used in a photolithography process; two of them are the photoresist and the developer. A photoresist is a light-sensitive material made up of a solvent, a polymer, and a sensitizer. When areas of the resist are exposed to light, the polymer structures of the resist change. In a positive photoresist, a photochemical process will reduce the length of the polymer chains, increasing the solubility of the resist allowing a developer to remove it. On the other hand, for a negative resist, the polymers in the exposed resist will cross-link, decreasing the solubility, leaving the unexposed part to be removed. Figure 2.6 summarise the difference between a negative and positive photoresist. The intensity of the light needed for proper exposure is given as energy per area mJ/cm^2 and depends on both the substrate and type of resist, making it necessary to perform an exposure test before final patterning [34].

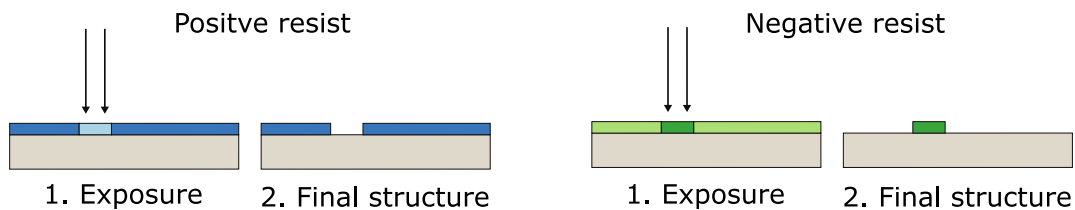


Figure 2.6: Simplified illustration of a positive and negative photoresists. A positive resist will become soluble by exposure and can be removed by a developer. The solubility of a negative resist will decrease after exposure, and the unexposed part can be removed. Adapted with permission from [35].

The developer is a chemical used to remove the soluble resist from the wafer. Depending on the type of resist, different processes occur during development. In a positive

resist, for instance, chemical reactions occur in order to remove the resist. For a negative resist, on the other hand, the soluble parts are not cross-linked and removed easier, and therefore, no chemical reactions are necessary, and the developer washes the resist away. Two measures of development are crucial, the selectivity indicating the developer's ability to remove the soluble resist and not the res, and the dissolution rate, indicating the speed of development. A developer with high selectivity and dissolution rate is desirable. Although, a too high rate is undesirable as it can make Repeatability difficult if small variations in development time affect the process. As the dissolution rate may vary depending on the resist and temperature, experiments involving development time should be performed to avoid over- or underdevelopment [34].

2.7.2 Process flow

Figure 2.7 shows the flow of a "typical" lithography process where each section is described in further detail below. Although the steps presented can occur during a typical process, some steps are not necessary for some processes. Especially some of the baking procedures are not used for every resist [34].

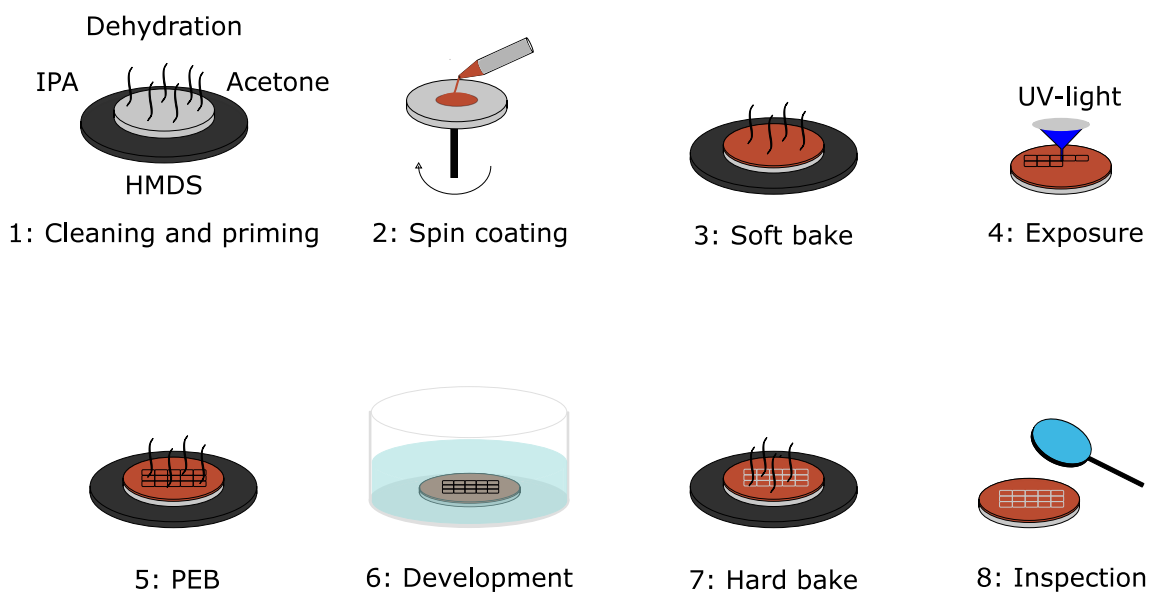


Figure 2.7: An illustration indicating different steps that can occur during an optical lithography process. Some steps are required, such as exposure and development, while others are not always necessary, such as post-exposure bake (PEB) or hard bake.

1: Cleaning and priming Substrate cleaning is the first step of the process and is highly important as it removes contaminants from the substrate that can cause problems during resist deposition. Cleaning is often performed by submerging

the wafer in acetone that removes most contaminants, followed by isopropanol, as acetone can leave residue on the surface when it evaporates.

In order to achieve proper adhesion between the substrate and the resist, it is essential to remove any humidity as the photoresist is highly hydrophobic, and any water on the wafer will decrease the adhesion drastically. Dehydration is performed by heating the wafer, either through contact heating on a hot plate or in an oven.

Not all resist will adhere to all wafers' surface equally due to difference in hydrophobicity. By adding HMDS to the surface, it becomes more hydrophobic, and hence the resist, which is also hydrophobic, adhere much better to the wafer. When HMDS is added, it chemically bonds to the wafer's surface, adding a hydrophobic hydrocarbon chain to it. This process can be performed in a desiccator which will evaporate the HMDS, allowing it to bond with the wafer [34].

2: Spin coat Spin coating is an often-used technique to distribute an even film of photoresist on a wafer. A puddle of resist is deposited on the substrate, followed by a high-speed spin, which distributes the film on the substrate evenly. Spin speed and spin time contribute to the thickness and uniformity of the resist and varies with the substrate and resists.

3: Soft bake After spin coating, a soft bake is performed to remove solvent from the resist, as the solvent's purpose is to distribute the resist on the wafer evenly. By performing this step, water and solvent evaporates and improves the adhesion of the photoresist.

4: Exposure During exposure, the resist is exposed to UV light in a pattern given by the user. There are two common ways of exposing the sample, using a mask-aligner or a maskless aligner. A mask-aligner utilises a pre-made mask. UV light is transmitted through the open areas of the mask, which causes the pattern of the mask to transmit to the resist. This is a fast and effective way of exposure but is very rigid as changing the mask demands considerable work.

A maskless aligner, on the other hand, uses an spatial light modulator (SLM), a combination of mirrors and lenses, in order to directly write a pattern given in a design file on the substrate. This technique is highly effective for exploring different mask designs, as the design only needs to change in the input file. The technique may be a bit slower than contact mask alignment but will also be much more versatile [36]

5: Post-Exposure bake After exposure, some resist-types demand a new thermal step to amplify the chemical process initiated by the exposure.

6: Development Development is the final fabrication step in the lithography pro-

cess. Here the soluble resist is removed, while the non-soluble resist is retained on the wafer.

- 7: Hard bake** After the pattern has been created, some resist demands a hard bake to stabilise the resist, further removing solvent from the resist.
- 8: Inspection** The last step of the photolithography process is inspecting the sample to view the final result of the process. Three types of resist profiles can be achieved after lithography and are presented in figure 2.8. An undercut profile is typical for negative resist, while an overcut profile can occur with positive resist. The vertical profile can be viewed as the "perfect" results but is hard to achieve. Often, undercut or overcut can be more suitable for specific processes; for instance, can an undercut profile help during metalisation and lift-off to avoid metal edges in the pattern.

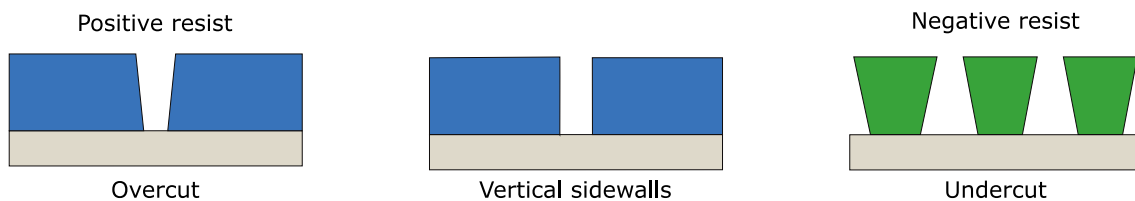


Figure 2.8: Schematic illustration of three different resist profiles from a lithography process. Negative resist often result in an undercut profile, while an overcut profile is normal for positive photoresist. Vertical sidewalls are hard to achieve but are considered the "perfect" resist profile. Adapted with permission from [35].

2.7.3 Metalisation and lift-off

After the resist pattern has been achieved through photolithography, metalisation and lift-off can be carried out to achieve metal structures on the substrate. Figure 2.9 shows a typical metalisation process. The metal is deposited on the substrate containing the resist before chemical methods are used to remove resist, leaving metal structures on the substrate. Several methods can be used for metalisation; for instance, sputter coating, evaporation, electroplating or metal chemical vapour deposition (CVD), and which should be used depends on the material, thickness desired, as well as what is most suitable for the design [34].

2.8 Electron beam lithography

Another form of lithography is electron beam lithography (EBL). Here, instead of photons, electrons are used to form patterns in the resist. The process is similar to the photolithography process explained in the previous section, although optical exposure is exchanged with an EBL. Just as explained for optical microscopy, the wavelength of

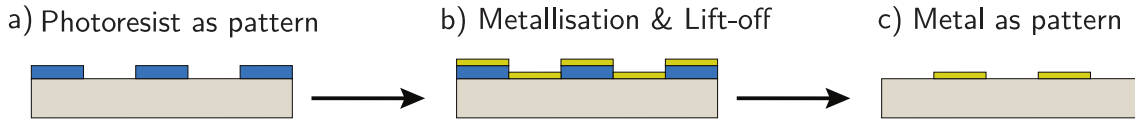


Figure 2.9: Simplified illustration the metalisation and lift-off process. a) Resist pattern is created, here with vertical sidewalls. b) Metal is deposited on the sample, leaving metal both on top, and within the pattern of the resist. c) Lift-off is performed, removing the resist with the metal, leaving patterns of metal on the substrate. Adapted with permission from [35].

light limits the feature sizes photolithography can achieve due to the diffraction limit. For that reason, electrons have been found as a decent alternative to lithography, in the same way as an SEM can be used instead of optical microscopy. The working principle of an EBL is the same as with an SEM. Electrons are accelerated towards the sample using an electron gun with accelerating voltage of 10 kV to 100 kV, and thereafter guided and centred using a system of electromagnetic lenses. As with an SEM, the resolution is not limited by the electron's wavelength but rather by aberrations in lenses and spot-size of the beam [36].

A few differences between optical lithography and EBL is vital to note. First, finding the correct beam current, voltage, write field size, as well as finding the exposure dose has to be done, and optimised, for the pattern and resist used. Also, due to the proximity effect, where electrons scatter within the resist, unwanted exposure to other parts will occur. This can, however, be corrected to a certain extent by adjusting the exposure dose for different areas of the resist, and computational methods have been made for this use [37]. Also worth noting, as the resist is exposed using a single beam source, exposing large patterns can be very time-consuming, and this has to be considered during planning [35].

2.9 Electron Beam Evaporation

Electron beam evaporation (EBE) is a physical vapour deposition (PVD) process in which particles, in this case, electrons, is used to evaporate atoms from a specific material. The evaporated metal is subsequently deposited on the desired substrate as a thin film. The technical aspects of an E-beam evaporation are shown in figure 2.10. A large potential difference, in the kV-range, is applied between a filament carrying a current and an area containing a magnetic field. This accelerates electrons towards the magnetic field, which guides the electrons towards a crucible containing the metal of choice. The atoms from the metal will then evaporate towards the substrate, where it is subsequently deposited. The entire process takes place within a vacuum chamber for several reasons. It allows for anisotropic deposition, maintains the electron beam, and avoids contaminations from gases such as O_2 . All the energy from the electrons carries over to heating the material, which allows for efficient evaporation without contaminants from other sources such as the crucible. It allows

for a deposition rate between 0.1 and 100 Å per minute, making it highly versatile. The EBE is often used for high precision coating of metals with a high melting point [38].

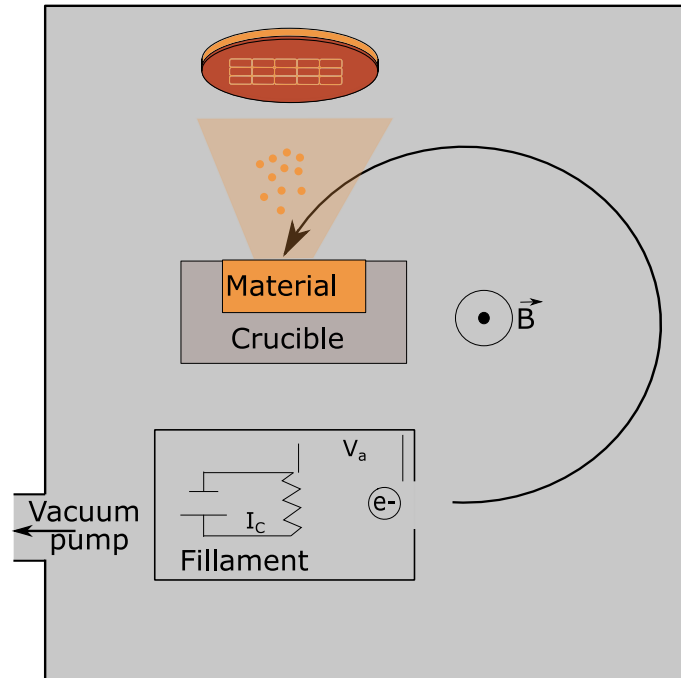


Figure 2.10: A simplified illustration of an electron beam evaporation (EBE) process. Electrons are generated from a current I_c in the filament and accelerated towards a magnetic field with a voltage V_a . The magnetic field B will then guide the electrons towards the material of choice, which is evaporated on the sample. All this occurs within a vacuum chamber.

2.10 Wire bonding

In order to electrically connect the fabricated micro-circuit to another system, wire bonding is commonly used. A wire of conducting metal, often gold, is attached between parts of two separate circuits. There are several different bonding techniques, such as thermocompression bonding, ultrasonic bonding and thermosonic ball bonding. These techniques are differentiated on how they attached the wire to the pad.

Thermocompression bonding uses heat and pressure, ultrasonic bonding uses pressure and ultrasonic energy, while thermosonic ball bonding uses all of these. Both ultrasonic sound, pressure and heat, in order to attach the wire to the pad. What technique should be used depends on the material as well as the packaging of the fabricated circuit.

Thermosonic ball bonding is often used as long as the sample and packaging can withstand both heat and ultrasonic vibrations. Figure 2.11 shows how the process

works. A ball of molten metal is created at the tip of the wire either through a flame or electric discharge. This is then placed on the heated contact pad, where ultrasonic vibration and pressure is applied. Metal bonds are then formed between the ball of the wire and the sample pad. In the end, the wire transferred to the packaging pad and is attached using the same procedure and broken off, creating a wire between the two pads. The applied force ultrasonic frequency and heat depends both on the substrate, composition and form of the pad, as well as the wire used for bonding. Hence after any substantial changes to any of these parameters, test bonds should be performed in order to find the perfect bond settings [34] .

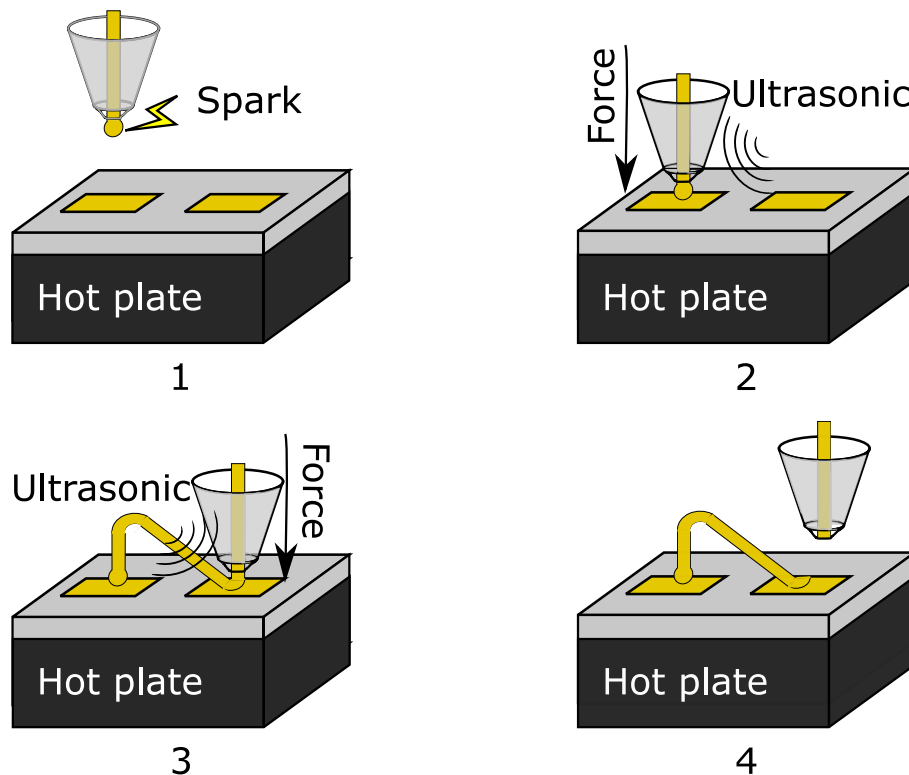


Figure 2.11: Illustration of a thermosonic wire bonding process, using a ball bonding tool. **1)** A spark causes a ball to form on the metal wire. **2)** A force F_1 pushes the wire on the contact, along with an ultrasonic frequency f_1 , and a temperature T causing metal bonds to form between the contact and wire. **3)** The wire is moved to the other contact and a new force F_2 , frequency f_2 and temperature T is applied, and again metal bonds are formed **4)** The wire is cut, and the process can be repeated.

3 | Experimental

3.1 COMSOL simulations

In this thesis, COMSOL Multiphysics was used for simulations of the system to optimise the characteristics of the fabricated heater. Using the properties presented in chapter 1, along with some educated guesses relating to the theory of resistivity and heat transfer, a structure was designed using COMSOL's geometry compiler. Here, of importance was the ability to arrive at a design that can achieve high power close to the area of interest (AHA) area, while at the same time have close to lossless contacts for guiding the current. Therefore a design with a high disparity between the active heater area and contact area was devised. The design was made fully parameterisable to be able to perform tests on different dimensions of the heater.

After establishing a suitable design, meshing was performed, dividing the system into smaller elements. Some test were performed, changing the size of the elements until simulations could be performed within a reasonable amount of time. Here, it was chosen to use different dimensions of elements within different domains to minimise computation time. However, to achieve accurate simulations, small elements were used in corners, sharp edges, and the materials' boundaries.

As mentioned in chapter 2, the second part of COMSOL's workflow is adding the laws of physics that apply to the system. That is, what equations should COMSOL solve the system for. As the purpose of this simulation was joule heating, of interest was adding the electrical currents module and heat transfer in solids to the system. These were coupled through the multiphysics model. For each module, different physical phenomena were added, which supplied the system with the equations needed. Furthermore, for COMSOL to properly solve the equations, it needed boundary conditions. For that reason, a set of starting conditions were added that could depict a real-life system. Following below are the physics module as they were defined.

Heat transfer in solids:

- **Heat flux:** All boundaries have been set to have a convective heat flux to the

environment of $5 \text{ W/m}^2\text{K}$

- **Temperature:** The temperature of the environment was set to a parameter that can be changed called `start_temp`. Moreover, in order for the system to have conductive heat flux away from the system, the starting temperature was also set to the chip's edges. Allowing for conduction away from the system. In simulations, the start temp was set to room temperature (292 K).
- **Surface-to-ambient radiation:** Radiation from the material will have loss given by Stefan-Boltzmann law, which is added to the system. Here an emissivity $\epsilon = 0.7$ for silicon is used [39].

Electric currents:

- **Current conservation:** The current in the system should be conserved, and the resistivity was set to be temperature-dependent using temperature-dependent resistivity as explained in the theory section. The temperature coefficient $\alpha = 1.71 \times 10^{-8} \Omega \text{ m}$ was given by the predefined material properties in COMSOL.
- **Electric insulation:** Electrical insulation was set between the microheater and silicon, and the surrounding air.
- **Potentials:** A positive voltage V_0 and ground potential was defined on the contact pads for the heater. Throughout all simulations, this voltage was $V_0 = 5 \text{ V}$.

After all the physical aspects of the system had been defined, studies on the system were performed. Several different studies can be performed, but for this thesis, a few are of special interest, as described below:

- **Parametric study** A parametric sweep was performed to discover both how the system changes for a different set of values but also to arrive at parameters necessary to heat the AHA to roughly $100 \text{ }^\circ\text{C}$.
- **Stationary study** Having found the ideal parameters, the system's temperature and current were analysed using a stationary study, indicating the temperature for which the system stabilises.
- **Time-dependent study** A time-evolution simulation was performed in order to observe how the temperature changed over time and how long it took before stabilisation occurred.

3.2 Realisation of the proposed design

After simulation, the chosen design was actualised in NanoLab at NTNU. Fabrication was performed using photolithography followed by metalisation, lift-off, scribing and

wire bonding. The process was performed on 2" silicon wafers, having a crystal plane orientation of $\langle 100 \rangle$ and a resistivity of $0.5 \Omega \text{ m}$. The MLA150 Maskless Aligner from Heidelberg Instruments was used for exposure, while metalisation of copper was performed using a PVD 75 Custom E-beam Evaporator from K.J. Lesker.

The fabrication process was divided into three sub-processes. The first part consisted of obtaining the optimal photolithography parameters through dose and development testing. After that, lithographic fabrication of the heaters was carried out through metalisation. In the end, scribing and wire bonding was performed to attach the device to the correct carrier, which then could be used for characterising the thermal properties of the heater.

3.2.1 Photolithography - dose and development testing

Before performing the lithography process of the final design, the correct parameters such as development time and exposure dose had to be determined. Lift-off was used after metalisation, which generally would indicate the use of a negative photoresist due to the possibility of achieving an undercut profile. Despite this, both positive and negative photoresist were tested during this project, as the positive photoresist available is easy to handle, and the metalisation structures will be much smaller than the thickness of the photoresist, making it easier to perform lift-off without undercut. Furthermore, it is often easier to achieve high resolution using a positive resist [34].

The wafer was cleaned using acetone and isopropanol (IPA), followed by plasma cleaning using the TePla 300 Plasma asher. Resist was deposited through spin coating, and the thickness of the resist was measured using the Filmetrics F20 reflectometer.

Two-inch silicon wafers were used for dose and development testing, and several copies of a dose design were exposed on the wafer. After that, the wafer was cut into several pieces, and each piece was developed for a certain amount of time. Figure 3.1 shows the masks used for dose testing. Here, the design in figure 3.1a was used for positive resist, and while the design in figure 3.1b was used for the negative resist.

Negative resist process

ma-N 440 (Micro Resist Technology GmbH) was chosen as the negative photoresist as it was readily available at NanoLab and have an easy lift-off process using acetone. In figure 3.2 the process steps of using ma-N 440 for photolithography is shown. The recommended developer, ma-D 332 (Micro Resist Technology GmbH), was chosen to use during development. Furthermore, the different steps have been chosen by reviewing the datasheet of the resist [40].

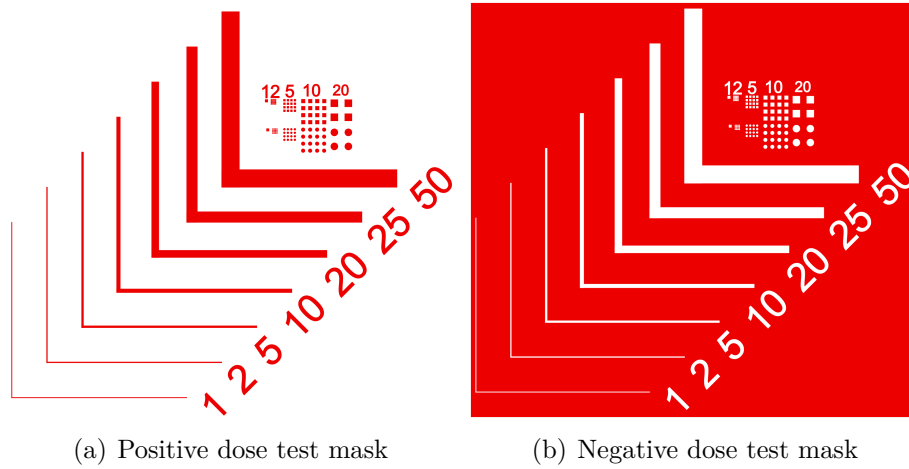


Figure 3.1: The design used for dose and development testing. figure a) Shows the mask used for the positive resist while figure b) shows the mask used for a negative resist. Design has been supplied by Mark Chiappa at NTNU NanoLab.

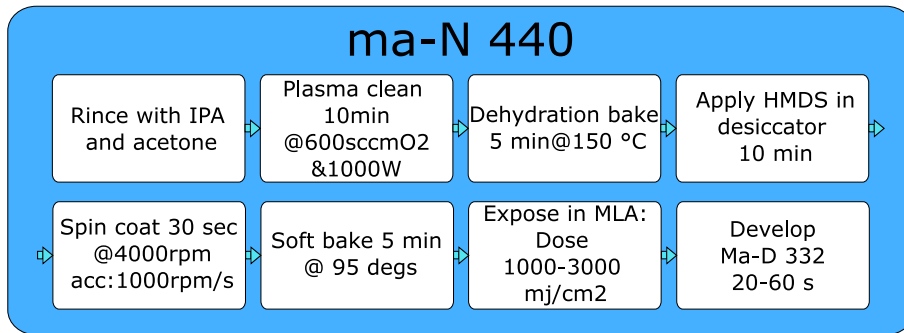


Figure 3.2: Diagram of all the steps used in the photolithography process with ma-N 440 as the resist. Exposure was performed with doses ranging from 1000 mJ/cm² to 3000 mJ/cm² and development was done using ma-D 332 for 80 s to 120 s.

Positiv resist process

For lithography using a positive photoresist, MEGAPOSIT™SPR™700-1.0 (SPR700) was chosen as it too is readily available in NanoLab and was recommended by staff due to its consistency and ease of use. For development, ma-D 332 was chosen for SPR700 as the recommended developer contains TMAH, a hazardous chemical that is beneficial to avoid for a simpler process. After suggestions from NanoLab staff, the developer was mixed with deionised water in a 70 % developer 30 % water mixture. This was done to reduce the dissolution rate to increase the accuracy. The datasheet of the resist was used to define the rest of the parameters, and the process can be viewed in figure 3.3 [41].

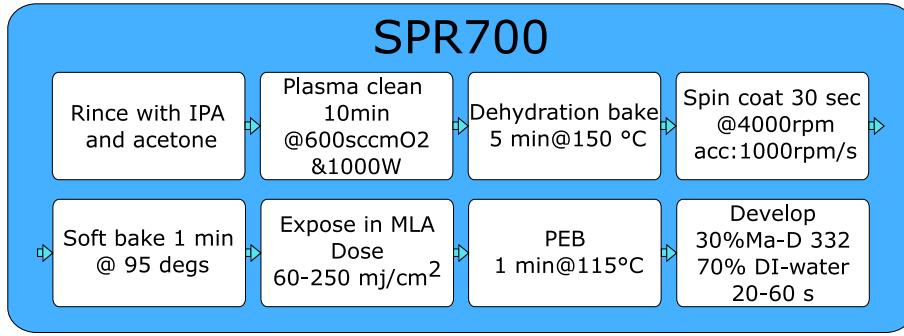


Figure 3.3: Diagram of different steps performed in the positive photolithography process using SPR700 as the resist. Exposure was performed with doses ranging from 90 mJ/cm^2 to 150 mJ/cm^2 and development was done using a diluted solution of ma-D 332 for 20s to 60s.

Table 3.1: An overview of the different parameters used for electron beam evaporation, both for fabrication of the heaters as well as the for the magnets. In this table current is the current of the filament, voltage is the accelerating voltage of the electrons, rate is the deposition rate and thickness is the amount of material deposited.

	Heater structure			Magnets	
	Ti	Cu	Al	$\text{Ni}_{0.8}\text{Fe}_{0.2}$	Al
Thickness	5 nm	145 nm	5 nm	10 nm	2.5 nm
Rate	3 \AA/s	5 \AA/s	3 \AA/s	2 \AA/s	1 \AA/s
Current	120 mA	330 mA	410 mA	36 mA	110 mA
Voltage	10 kV	10 kV	10 kV	8 kV	8 kV

3.2.2 Physical realisation of micro heaters

After the optimal parameters of the lithography process were found, the heater could be fabricated. During dose and development testing, it was decided that SPR700 should be used as the resist, and the same procedure used in dose and development testing was employed during this step. The exposure dose used for this step was 110 mJ/cm^2 while development was performed using 70% ma-D 332 and 30% water for 40s, after analysing the dose and development test. See chapter 4 5 for further information.

After photolithography, metallisation was performed using an electron beam evaporator. A layer of 5 nm Titanium was first deposited in order to improve adhesion between copper and silicon [42]. Subsequently, 145 nm copper was deposited, followed by 5 nm aluminium to minimise oxidation of the structure. The different parameters used in the deposition, such as filament current, deposition rate and accelerating voltage, can be found in table 4.1. After metalisation, lift-off was performed using acetone, combined with an ultrasonic bath and a small brush to help the process further.

3.2.3 Fabrication of micromagnets

An array of micromagnets was fabricated within the heaters, each having a size of $1\ \mu\text{m} \times 10\ \mu\text{m}$. During this fabrication, SPR700 was chosen as the resist, and hence the same lithography process as used in previous steps was used here. The structures were aligned with the previous design and exposed with $110\ \text{mJ}/\text{cm}^2$ and developed for 40 seconds using 70% Ma-D 332 and 30% water. Furthermore, metallisation was carried out using the Vacuum Classic 500 E-beam evaporator from Pfeiffer. For the magnetic material a 10 nm layer of $\text{Ni}_{0.8}\text{Fe}_{0.2}$ was deposited followed by 2.5 nm thick layer of Al was to minimise oxidation. Lift-off was performed using acetone in an ultrasonic bath.

3.2.4 Fabrication of nanomagnets

Several ASI-structure and stand-alone nanomagnets, with dimensions of $80\ \text{nm} \times 220\ \text{nm}$ were fabricated within the heaters due to the micromagnets not being mono-domain. See chapter 4 and 5 for further information. During this process, electron beam lithography (EBL), by the ELS-G100 EBL from Ellionix, was used to expose the resist, and as this process has been perfected by the group already, there was no need for dose and development testing. Here, the E-beam resist used was AR-P 6200 (CSAR 62) from Allresist GmbH, followed by development using AR 600-546 from the same manufacturer. The full lithography process is given as a diagram in figure 3.4. Proximity effect correction was performed using the Beamer software from GenISys GmbH, giving an exposure dose in the range of $250\ \mu\text{C}/\text{cm}^2$ to $350\ \mu\text{C}/\text{cm}^2$. The beam current was set to 500 pA

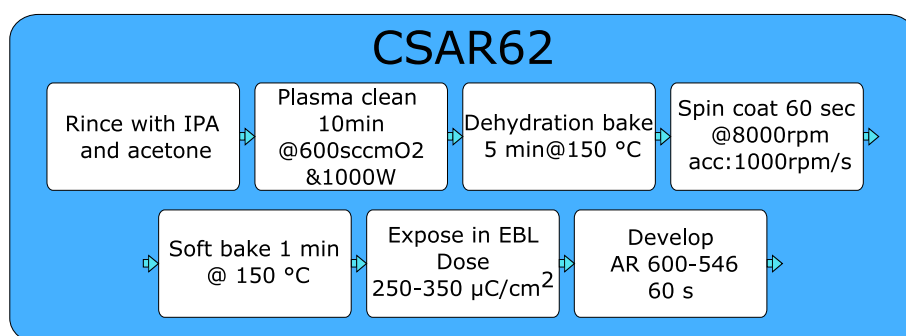


Figure 3.4: A diagram showing the different steps for the electron beam lithography process. Exposure was performed with a dose of $250\ \mu\text{C}/\text{cm}^2$ to $350\ \mu\text{C}/\text{cm}^2$ and development was done using AR 600-546 for 60 s.

After EBL, metallisation was performed, again the EBE from Pfeiffer was used, and 10 nm of $\text{Ni}_{0.8}\text{Fe}_{0.2}$ followed by 2.5 nm Al was deposited using the same parameters as for the micromagnets, as presented in table 4.1.

3.2.5 Characterisation of the fabricated structures

Characterising the structures was performed using both an optical microscope, an SEM and a profilometer. For dose and development testing, the brightfield settings of Zeiss AxoScope A1 from Carl Zeiss was used to evaluate the results, while the metalised heaters and magnets were characterised in the APREO SEM from FEI. The thicknesses of the heaters was also measured using the Veeco Dektak 150 profilometer from Veeco.

3.2.6 Scribing and wirebonding

In order to connect current and voltage to the microheater, the chip was attached to a carrier. For this project, two different carriers are used, as they are specifically designed to match the different characterisation tools used in the group. A leadless chip carrier (LCC) is used for applying current in the three dimensional rotator (3DR) which have 20 connections, while a printed circuit board (PCB) is used in the magnetic force microscopy (MFM) and offers only 4 connections.

As the designs are fabricated on 2" silicon wafers, it is necessary to cut the wafer into smaller pieces suitable for the different carriers. The scribing was performed using the MA-100 manual wafer scribe from Süss to achieve accurately shaped chips. The size of the final chip was 4.5 mm and was attached to the carriers using copper tape.

Wirebonding was performed using HB05 Wedge and Ball Bonder from TPT, using the ball tool. In order to find the perfect settings, several test bonds were performed, and the final bond settings are shown in table 3.2.

Table 3.2: The different settings used during wirebonding of the final design.

	Bond 1	Bond 2
Ultrasonic	190 kHz	262 kHz
Time	200 ms	205 ms
Force	36 g	40 g
Temperature	94 °C	94 °C

3.3 Characterization of heating

In order to evaluate the thermal properties of the device, resistivity measurements on the heaters were performed using the 3DR. One heater was connected to a voltage source, while another was connected to an Ohmmeter. An illustration of the setup can be viewed in figure 3.5(a). While a voltage ranging from 3 V to 33 V was applied to the circuit named C_h^{3DR} , the resistance of the other circuit, C_m^{3DR} , was measured.

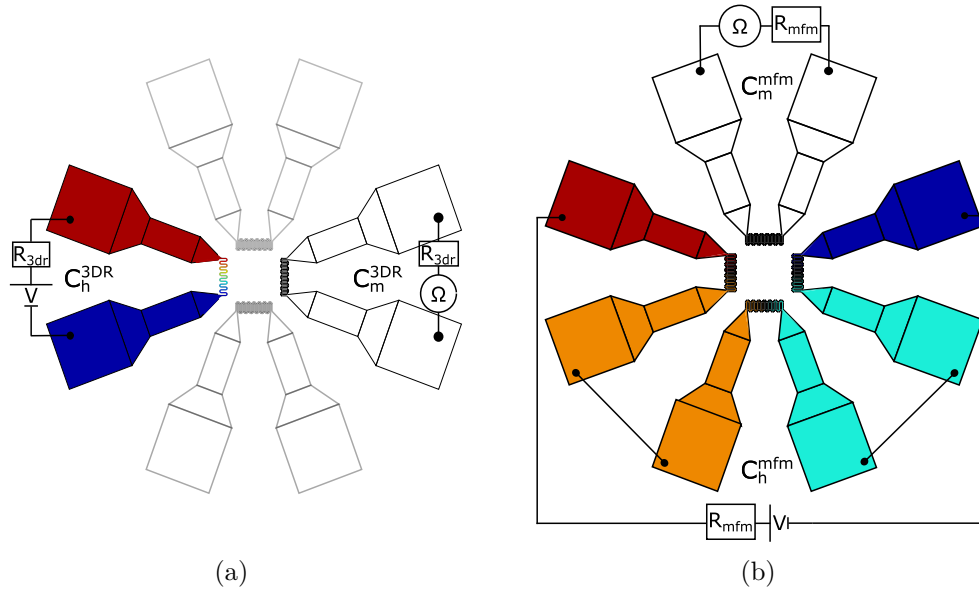


Figure 3.5: A circuit diagram showing how the heaters are connected during evaluation. **a)** The circuit of the chip in the 3DR. One heater is connected to a power source, applying a voltage V and having a load resistance R_{3dr} from the 3DR. This is called the C_h^{3DR} circuit. The other is connected to an ohmmeter from a source meter unit (SMU), having the same load resistance and is called C_m^{3DR} . **b)** The circuits of the MFM-measurements. Three heaters are connected in series and connected to a voltage source applying a voltage V . This circuit is named C_h^{mfm} . The last heater is connected to an ohmmeter for measuring the resistance while voltage is applied to the other three. This circuit is named C_m^{mfm} . Both circuits have a load resistance of R_{mfm} .

Between each time a voltage was applied, the voltage was turned off, and the heater was cooled down to room temperature. Furthermore, the change in resistance was translated to a temperature using equation (2.3).

3.3.1 Magnetic measurements

In order to evaluate how the temperature affects the magnetic properties of permalloy magnets, measurements in an MFM were performed. The PCB, with a chip containing heaters and magnets, was cooled down to 4 K using a cryogenic cooler. For this test, three heating elements were used for heating, the C_h^{mfm} circuit, while the last heater, in the C_m^{mfm} circuit, was used to measure the resistance, and hence the temperature. An illustration of the circuits is shown in figure 3.5(b).

Before any magnetic measurements were performed, a calibration using the built-in heater was used to measure resistance at specific temperatures. Temperatures ranging from 5 K to 100 K was applied to the system, and resistance measurements were performed. This could then be used to indicate what resistance the circuit have at specific temperatures.

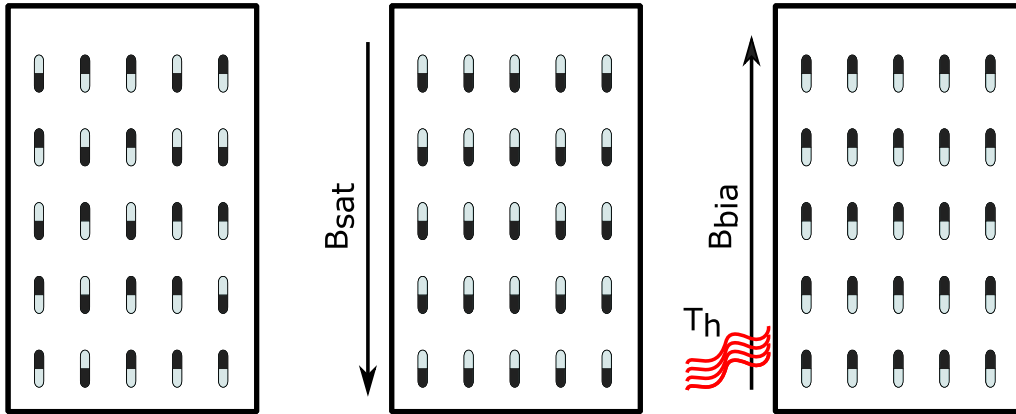


Figure 3.6: A diagram showing how the magnetic measurements were performed using in the MFM. The magnets are first initialised with a magnetic field B_{sat} forcing all magnets to point in the same direction as the magnetic field. A bias field B_{bia} is applied in the opposite direction of the B_{sat} field along with a temperature T_h given by the heaters. The voltage/temperature is increased until the magnetisation of the magnets flip. Different bias fields are tested to observe how the coercivity of the system changes with temperature.

Stand-alone magnets, not magnetically coupled, was fabricated within the heaters, and MFM measurements were performed. An illustration of how these measurements were performed are given in figure 3.6. First, A magnetic field $B_{sat} = -0.1$ T are applied to magnets pointing in random directions, magnetising them in the direction of the magnetic field. Then a bias field B_{bia} ranging from 0 mT to 50 mT was applied along with heat from the heaters supplying a temperature T_h to the system. A voltage in the range of 3 V to 33 V applied to the C_h^{mfm} circuit, as illustrated in figure 3.5(b), was used to generate the heat from the heaters. Between every operation, an MFM was used to measure the magnetisation of the magnets. This then shows how much voltage, or temperature, is necessary to flip the magnetisation of the magnets. This indicates how the temperature affects the coercivity of the system. During all this, the resistance of the last heater, the C_m^{mfm} circuit was measured to indicate the temperature of the system during measurements.

4 | Results

In this chapter, the results gathered during this project will be presented. Firstly, we will look at the design created for this thesis and simulations performed using COMSOL Multiphysics. Subsequently, we present the results from micro- and nanofabrication, both the results from the development process and the final fabrication steps. Finally, we introduce the results from characterising the thermal properties of the final device.

4.1 COMSOL Simulations

Creating the heater design

In the introduction, a few desired properties for the heater was presented. Most notably, it should be able to heat a local area of approximately $200\ \mu\text{m} \times 200\ \mu\text{m}$, relatively fast and evenly. With that in mind, the design given in Figure 4.1 was created. There are four separate heaters in this design, each capable of delivering heat to the area of interest (AHA) individually. Four heaters were chosen for symmetry purposes, as the design would distribute an even temperature to the entire area. Furthermore, by having separate heaters, it is possible to solely apply current to one of the heaters to create a temperature gradient across the active heating area. The design was first based on an educated guess, then further optimised based on simulations.

Each heater consisted of two main parts, the contact pads, two for each heater, and the main heating element. The entire chip with the heater and the large contact pads can be seen in the leftmost part of figure 4.1, while the rightmost part shows an enlarged part of the design, displaying the main heating element. For the heater to generate heat close to the AHA, the total area of the main heating element is held much smaller than the rest of the heater.

It was chosen to use copper for the heater material because it has high conductivity and will therefore be close to lossless in the contact pads and be cheap and easy the deposit. The substrate was chosen to be silicon as this is the substrate used for the artificial spin ice (ASI) structures in the group.

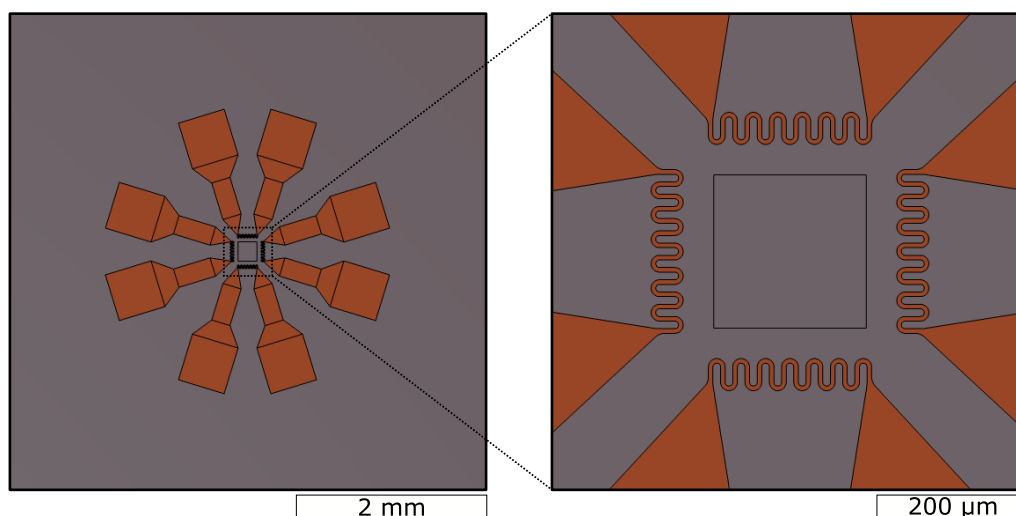


Figure 4.1: Illustration of the design created and evaluated during this thesis. The leftmost figure displays the entire system consisting of four separate heaters deposited on a silicon substrate. Each heater consisted of contact pads and a main heating element that should allow for uniform heating of a small area of about $200 \times 200 \mu\text{m}$. the rightmost figure shows an enlargement of the central part of the heater, displaying the main heating elements and the AHA.

Parametric simulations of the proposed design

Different dimensions of the heater were tested to identify a design that increases the temperature of the AHA to the desired value. For this reason, the design was made fully parameterisable, meaning every aspect of the design could be changed and remain coherent. These parameters are presented in figure 4.2. In the leftmost figure, the parameters relating to the contact pad are shown, while an enlarged illustration of the main heater and its parameters is given in the rightmost figure. Throughout the thesis, the size of the contact pads and the total chip size was kept constant in all simulations and fabrications. The size of the contact pads was chosen in order to easily wire bond the heater from the circuit to the printed circuit board (PCB) and leadless chip carrier (LCC), while simultaneously keep the entire chip less than $4.5 \mu\text{m}$. This was necessary in order for the chip to fit in the LCC. Table 3.1 shows values of different parameters in the design, both the ones that were kept constant as well as the ones that were simulated with different values.

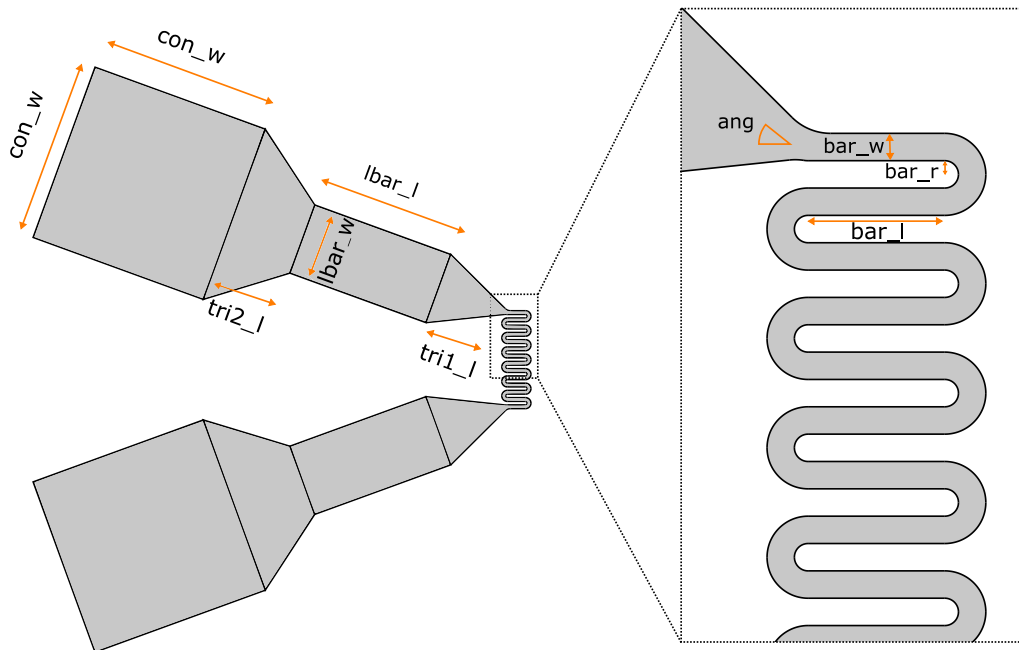


Figure 4.2: Illustration of the heater, along with the names of the parameters of the design. The figure to the left shows a full heater and the names of all the parameters making up the contact pad. The figure on the right shows an enlarged view of the main heating element along with its parameters.

Table 4.1: An overview of the different parameters, shown in figure 4.2, and values used in the simulations. The constant parameters are the ones that have been kept constant throughout this thesis. For the tested parameters, the range of the values that have been simulated is shown, and the chosen values were the values used for the final design. These were also the ones used for the physical realisation of the design.

Constant parameters		Tested parameters		
Name	Value	Name	Range	Chosen values
con_w	500 μm	bar_w	3-10 μm	6 μm
lbar_l	400 μm	bar_l	10-50 μm	20 μm
tri2_l	200 μm	Cu_h	100-300 μm	150 μm
tri1_l	200 μm	bar_r	3-6 μm	5 μm
lbar_w	200 μm			
ang	17°			

After arriving at an ideal design, a chosen set of parameters were tested to evaluate precisely how much the temperature of the AHA changes when the heaters dimensions change. In figure 4.3 the average temperature of the AHA, as well as the total current of the system, is plotted versus the dimension of the parameter. Figure 4.3(a) and 4.3(c) shows that increasing the bar length and radius increases the current and temperature. Moreover, increasing the copper thickness and bar width decreases these attributes, which is shown in figure 4.3(b) and 4.3(d). When increasing the width and radius, the number of bars in the main heating element was increased in order to keep the total area close to constant, at $200\ \mu\text{m} \times 200\ \mu\text{m}$, which corresponds to the sudden jump in current and temperature.

During simulations, it was decided that it would be beneficial to keep the voltage and not current constant, to avoid runaway heating as the resistance increases at higher temperatures. Therefore, the voltage for all simulations was kept at 5 V. As it is necessary to have heat conduction, the temperature of the edges are held at a constant temperature of 292 K (20 °C)

After simulations, a clear picture of how much the temperature and current changes with different parameters were achieved, and the final dimensions of the heater was decided. These chosen parameters are presented in table 3.1. It was also decided to keep the dimensions of the heater relatively large in order to have an easier fabrication process.

Steady state simulations of the chosen values

As the final parameters had been set, simulations on this design were performed. A standard simulation indicating how the final temperature of the AHA, as well as the rest of the chip, would spread is shown in figure 4.4. The two leftmost figures show the surface of the chip at two different scales, with the same temperature mapping. From these, one can observe that the temperature diffused towards the edges, as expected, as this was the area conduction occurred, removing heat from the system. Furthermore, the leftmost figure shows the temperature within the AHA plotted with a new thermal map. Here it is shown that this area stabilises at an even temperature of 372 K to 376 K. As the desired temperature was 100 °C, this is in line with the set requirements. It is, however, essential to note that it was not expected that this would be the exact temperature of the fabricated heater, but any temperature differences could be overcome by changing the applied voltage.

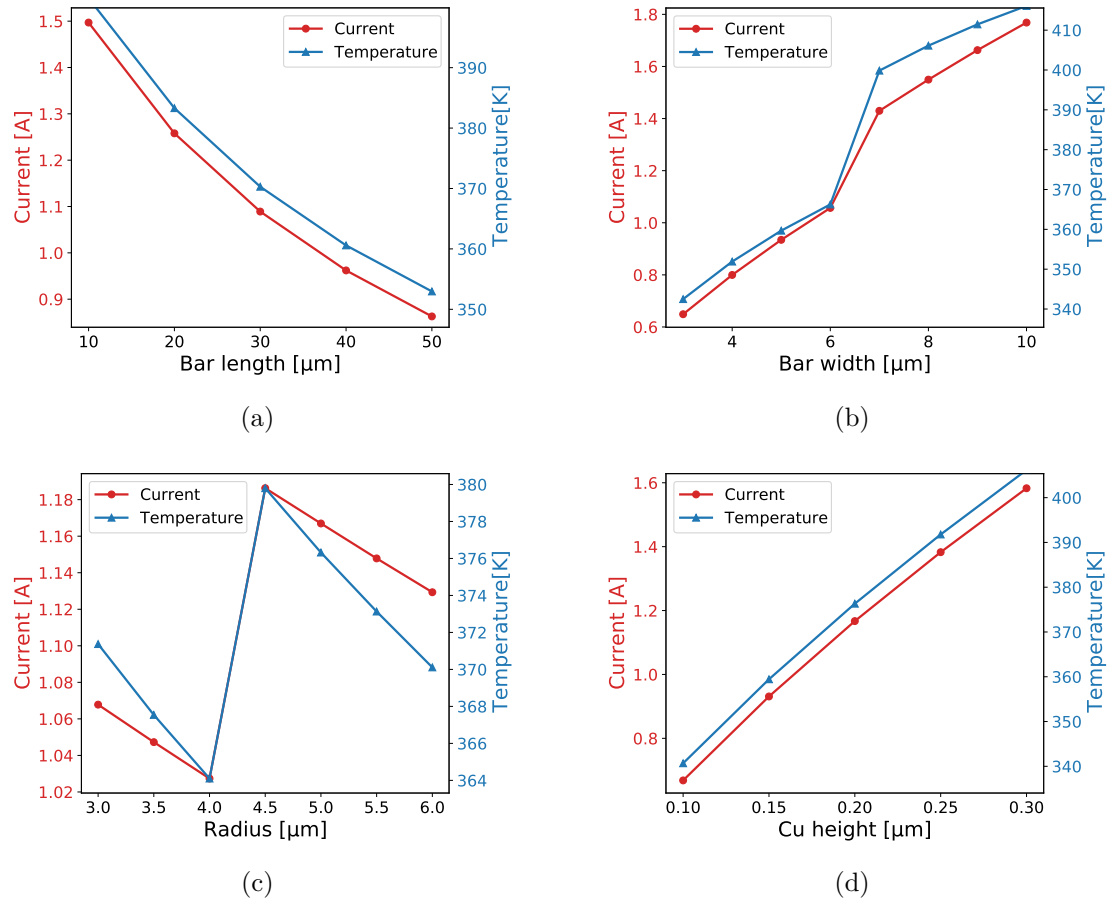


Figure 4.3: Plots of the average temperature of the AHA, as well as the current through the heater, when changing the dimensions of the heater. Note that the plots show the total current of all the heaters. Here the plots indicates a decrease in temperature and current with longer bars (a), or larger radius of the turns (c). While the current and temperature increases with wider bars (b) and thicker heaters (d).

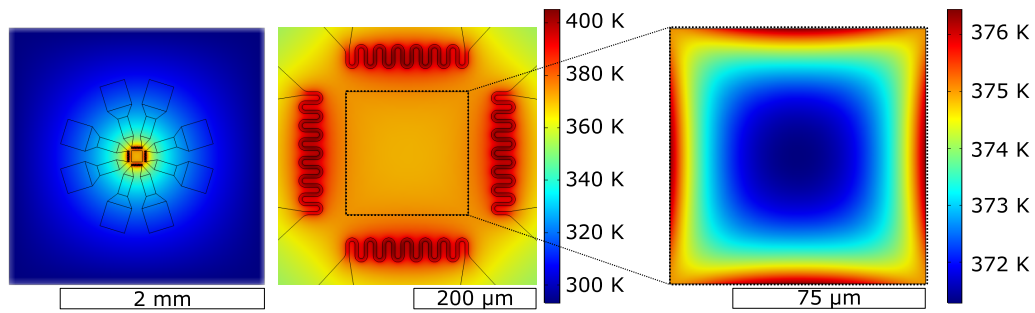


Figure 4.4: Thermal maps from simulations of the final design using COMSOL Multiphysics. The two leftmost figures show all heaters at different scales, illustrating the temperature gradient across the full system. Here the maximum temperature reaches 400 K within the main heating elements and decreases towards room temperature, 272 K at the edges. The map also indicates high uniformity of temperature within the active heating area. The rightmost figure shows the temperature of the active heating area, with a new, higher-resolution colour map. Here a temperature difference 3 K to 4 K within that area is shown.

Time-dependent studies of the proposed design

One important property of the heater was the ability to heat the AHA relatively fast, and therefore time-dependent studies were performed in order to simulate how temperature change with time. Plots from these studies are shown in figure 4.5. Here, both the temperature of the AHA and the current and resistance through one heater are plotted as they evolved over time. From these plots, it can be seen that already at 50 ms, the full system had reached a steady-state with a temperature of roughly 372 K, a resistance of 17.5Ω and a current of 0.283 A. In figure 4.6 snapshots of the surface temperature is shown, both for the full system in the leftmost figures and the AHA in the figure to the right. As one can observe from these figures, there are minimal changes to the AHA after 21 ms, indicating a fast stabilisation.

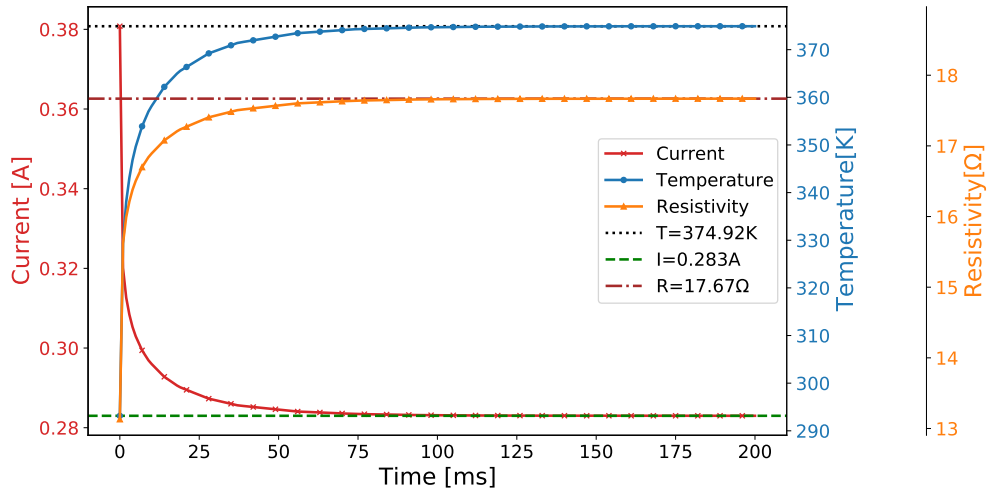


Figure 4.5: Plots showing the time evolution of the current and resistivity of one heater as well as the temperature of the AHA. In the legend, the maximum temperature and resistance, as well as the minimum current is added. The plots indicate a stabilisation of current and temperature after approximately 50 ms.

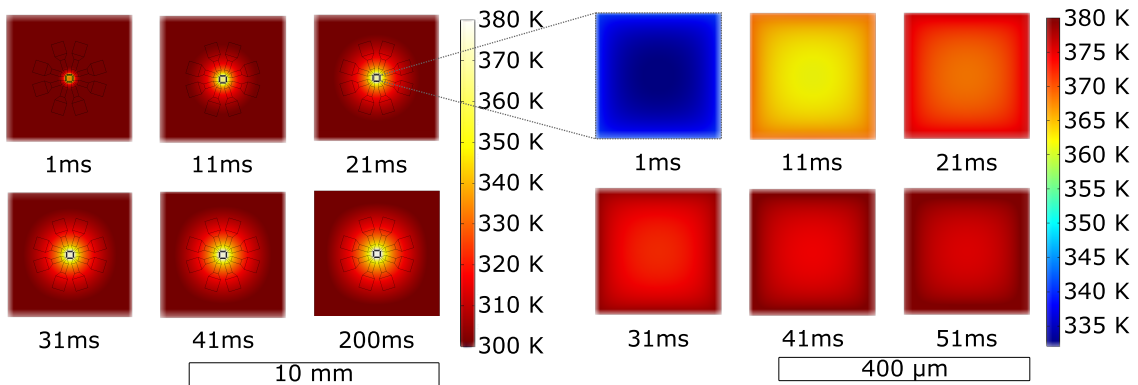


Figure 4.6: Snapshots of the temperature during time simulation at different times of the full system in the figures to the left, and the active heating area in the figures to the right.

4.2 Physical realisation of the system

After simulations had been performed and the results were acceptable, physical realisation of the system by means of lithographic techniques was performed. This section will present the results from the fabrication process, both of the heaters, as well as the micro- and nanomagnets. Firstly the results from dose and development testing will be introduced before moving on to the fabrication of the heater. After that, results from the fabrication of the micro- and nanomagnets is given.

Dose and development testing

To be able to develop a process that can fabricate heaters and magnets of different sizes, the ideal parameters for the lithography process had to be found. As both positive and negative resist should work for this design, both of these resist was tested. Figure 4.7 displays optical images of the resist patterns using the negative resist MaN-440, exposed with a dose of a) 500 mJ/cm^2 and b) 2500 mJ/cm^2 . For this particular test, development was performed for 80 s. The darker parts in these images are the resist, while the brighter parts are the wafer.

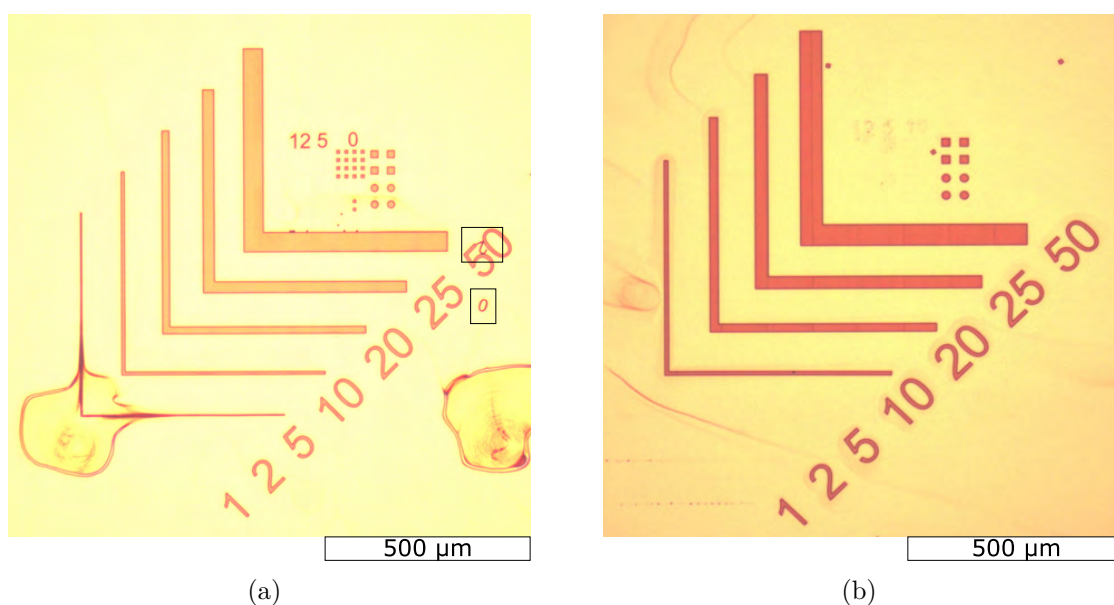


Figure 4.7: Optical images of MaN-440 resist patterns from **a**) using a dose of 500 mJ/cm^2 , and **b**) using a dose of 2500 mJ/cm^2 , where both have been developed for 80 s using Ma-D 332. From the marked areas in a, one can observe that some parts of the pattern have moved, indicating poor adhesion between the resist and structures.

There are two observations worth noting from these images. First, the sample does not appear fully developed as leftover resist remains on the sample. Secondly, the smaller features of the resist appear to have moved on the wafer. This can be

observed particularly in 4.7(a), as some numbers have moved to the middle right part of the pictured, as marked. This indicated that adhesion between the substrate and the resist was not adequate. It was, for this reason, decided that further work using ma-N 440 requires the use of HMDS to increase the hydrophobicity of the wafer, and hence, increase the adhesion.

In order to understand the relation between the exposed structure and photo dose, a dose test in the range of 1000 mJ/cm^2 to 3000 mJ/cm^2 for ma-N 400 was performed. This was combined with a test of development time in the range of 100 s to 140 s. The results from these test are displayed in figure 4.8. The array in figure 4.8(a) shows the optical images of results from the lithography process using different exposure doses and development times. Inspection showed that a sample exposed using a dose of 1000 mJ/cm^2 and developed for 120 seconds had the most promise. A magnified image of that sample is shown in figure 4.8(b), displaying lines supposed to be one and two micrometres wide. From this image, it is clear that both lines had been fully developed, but when comparing them to the scale bar, the lines appeared to be larger than expected.

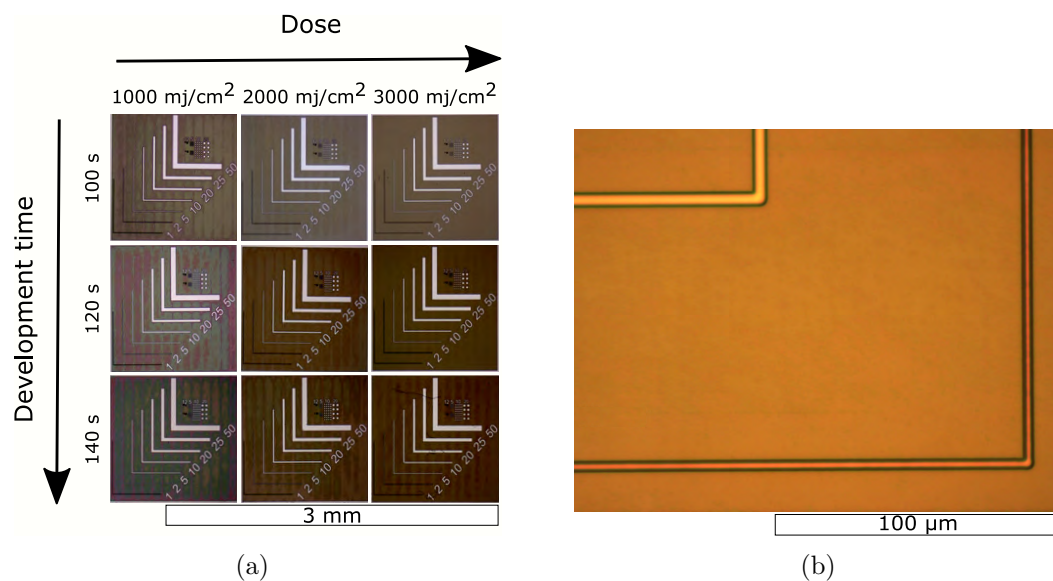


Figure 4.8: Optical images from dose and development testing using the the negative resist ma-N 440. **a)** An array of resist patterns after exposing the sample with doses of 1000 mJ/cm^2 to 3000 mJ/cm^2 and developing it for 100 s to 140 s. **b)** A magnified image of the 1000 mJ/cm^2 dose and 120 s development resist, showing the $2 \mu\text{m}$ and $1 \mu\text{m}$ line of the design. Comparing the result with the scale bar it may appear as the lines are too wide, indicating underexposure or over development.

After the negative resist was inspected, it was time to explore the positive resist SPR700. Another array containing different doses and development times of the test design is shown in figure 4.9(a). Already at low magnification, it is clear that development for 20 s is too short. The different colours in the design indicate that

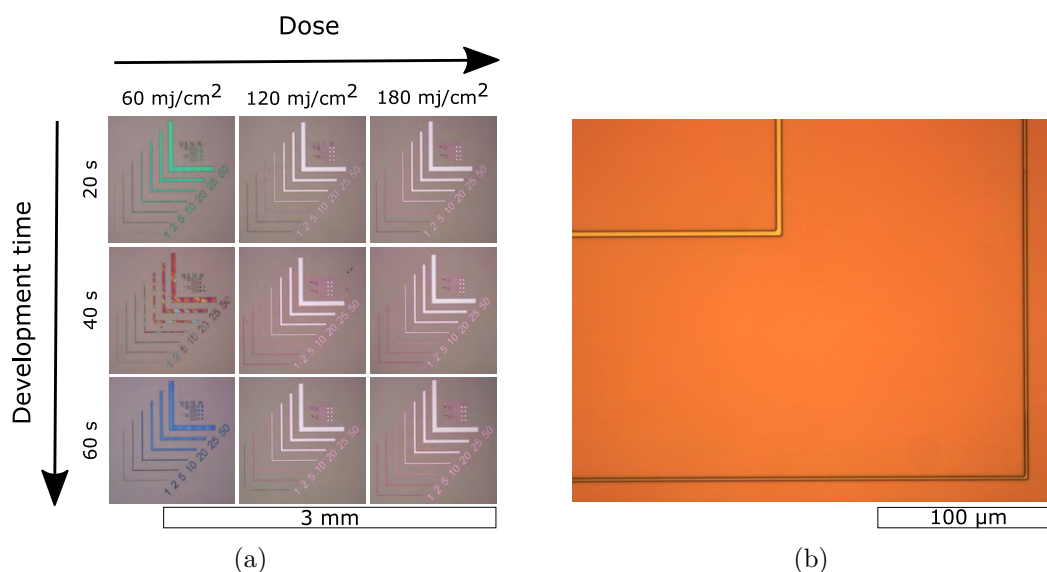


Figure 4.9: Optical images from dose and development testing using the the positive resist SPR700. **a)** An array of resist patterns after exposing the sample with doses of 60 mJ/cm² to 180 mJ/cm² and developing it for 20 s to 60 s. **b)** A magnified image of the sample exposed with a dose of 120 mJ/cm² and developed for 40 s, showing the 2 μm and 1 μm line of the design. The results indicates proper processing, as the lines appear open, but the width cannot be determined accurately using this characterisation technique.

there is resist residue within the lines, and therefore a development time of 20 s can be ruled out. Further observations of these results showed that a dose of 120 mJ/cm² and development for 40 s looks promising. An image of the one and two-micrometre line using a dose of 120 mJ/cm² and a development time of 40 s is shown in . Both of these lines look fully developed, and the line width seems reasonable when comparing it with the scale bar.

Due to some uneven development when using ma-N 440 and an easier and faster lithograph process using SPR700, as the need for HMDS is removed, it was chosen to focus on the positive resist for further process development. The design with the positive resist was inspected further in an scanning electron microscope (SEM) to view the exact line width of the design. From figure 4.10 one can observe SEM images of a dose of 120 mJ/cm² and development of 40s. figure 4.10(a) shows what should be a 50 μm line, while figure 4.10(b) shows the 2 μm line. Here one can see that the lines are approximately 1.5 μm thicker than the desired value, or in other terms, almost 75% larger than the 2 μm line. This might indicate a too high exposure dose or a too-long development time, and further testing using a lower dose and development time is necessary.

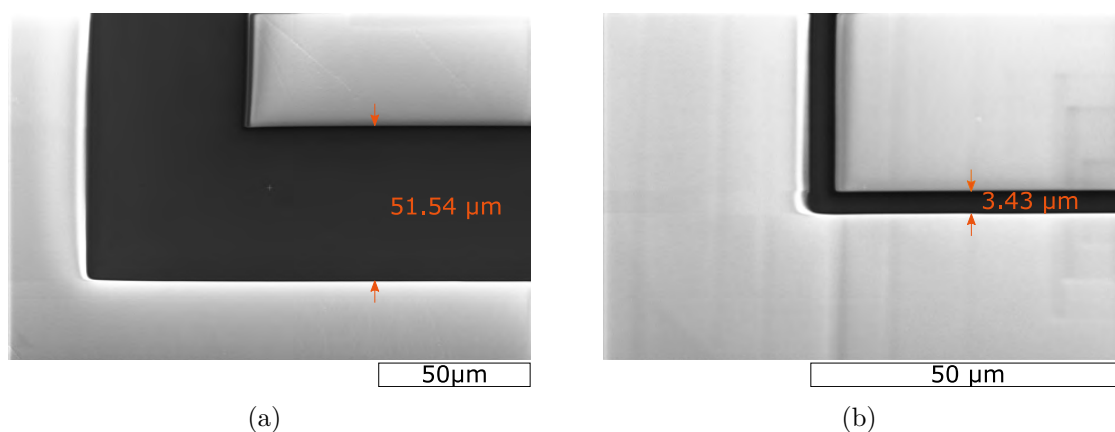


Figure 4.10: SEM micrographs of resist patterns exposed with a dose of 120 mJ/cm^2 and developed for 40 s. **a)** A $51.54 \mu\text{m}$ wide line measured using the SEM, that is supposed to be $50 \mu\text{m}$ wide **b)** A line supposed to be $2 \mu\text{m}$ wide from the design, that have been fabricated with a lateral dimension of $3.43 \mu\text{m}$, roughly 40% wider than anticipated.

For further evaluation of the optimal dose and development process, it was decided that metallisation and lift-off should be performed before inspecting the sample. This was done as it is easier to achieve more accurate images in the SEM, as charging will be less of an issue. Furthermore, it would be beneficial to observe how the metal structures would form for the different exposure and development parameters. Therefore 150 nm copper was deposited after lithography.

From these test, it was found that a dose of 110 mJ/cm^2 and development for 40 s yielded the optimal results. Figure 4.11 shows SEM images of the sample using these parameters, and from viewing the one- and two-micrometre line in figure 4.11(b) it is clear that in the vertical direction, the line-width is reasonably close to the design width. On the other hand, the horizontal part of this line does seem to be either overdeveloped or overexposed as the structures are too wide. A broader perspective of all the lines is shown in figure 4.11(a) while figure 4.11(c) shows fabricated squares and circles of different sizes. From these results, it can be determined that this particular lithography process should work for all dimensions down to the $2 \mu\text{m}$ scale. Therefore, it was concluded that the parameters given in table 4.2 should be used for further fabrications by SPR700.

Table 4.2: After dose and development testing, these were the parameters decided to be used for further lithographic fabrication using SPR700 as the resist.

Process step	Value
Spin coat	4000 rpm 30 s
Soft bake	1 min
Exposure dose	110 mJ/cm ²
Development time	40 s
PEB	1 min

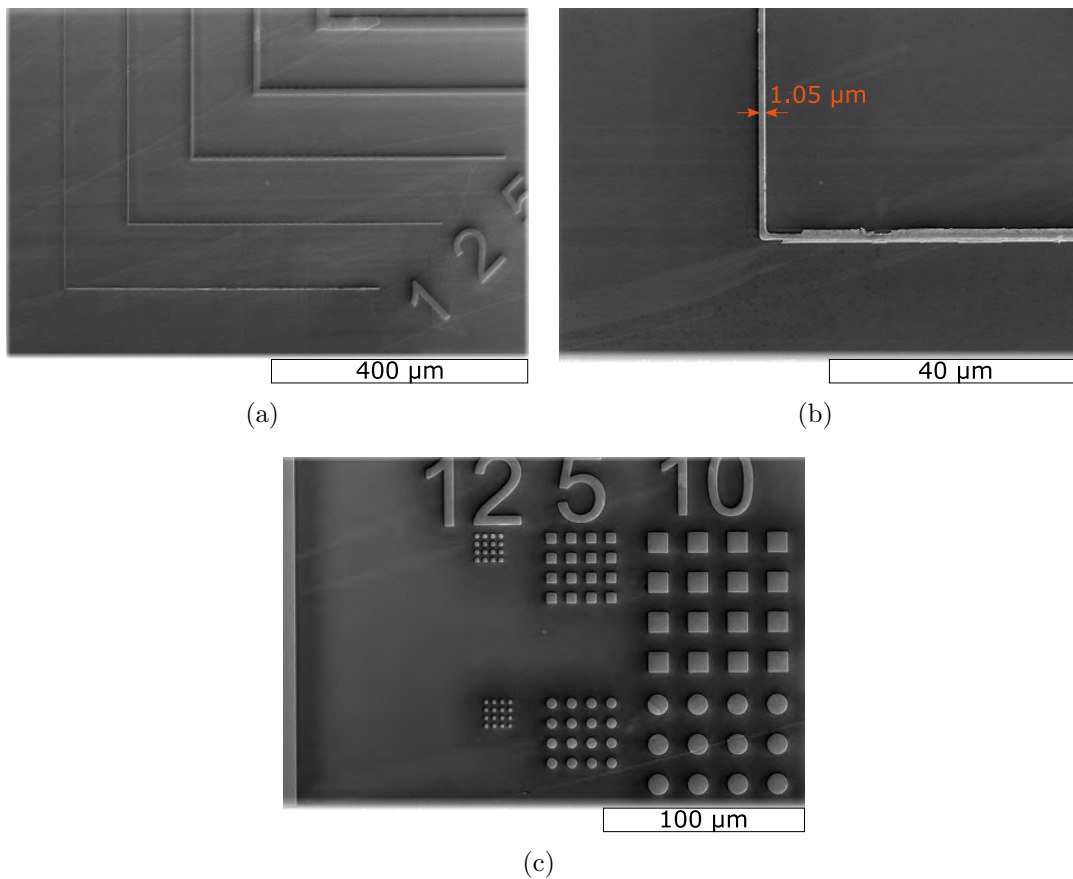


Figure 4.11: SEM images of copper structures of the test design, fabricated using photolithography and metallisation. SPR700 was used as the resist, and a dose of 110 mJ/cm² and development time of 40 s was used. **a)** Lines with different widths ranging between 50 and 1 µm. All lines appear fully fabricated. **b)** A magnified image of the 1 µm wide line along with a measurement taken using the SEM, indicating a width of 1.05 µm. The horizontal line appear to have a higher width than the vertical one **c)** Circles and squares with the number representing the different radii and side lengths of the structure. The only structures that have not been fabricated are the ones having a diameter/side length of 1 µm.

4.2.1 Using optimised lithographic process for fabricating microheaters

After both simulations and process development had been conducted, it was time to fabricate heaters. By using the parameters found during dose and development testing, as well as the design parameters found during simulations, several micro heaters were fabricated. SEM images of one of those are shown in figure 4.12. From these images, it is clear that the fabrication process works. The lines and turns are clear with no visible imperfections, and the dimensions are very close to the desired parameters presented in table 3.1.

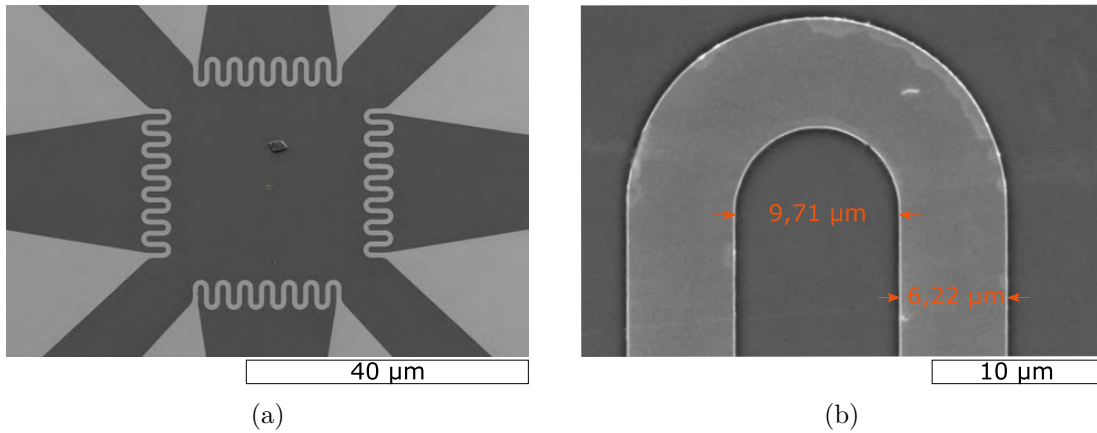


Figure 4.12: SEM images of the final heater manufactured in this thesis. a) All the four main heating elements. In the middle of the heaters, a small, particle, most likely dust can be seen. This have no effect of the final design as it can easily be removed by rinsing. b) A magnified image of the heater, along with measurements of the width of the bar and diameter of the turn. The values was measured using the SEM, and they are close to the chosen parameters presented in table 3.1.

By performing profile measurements using a stylus profilometer, the thickness of the heaters can be viewed in figure 4.13. Figure 4.13(a) is the profile of the central heating element, while figure 4.13(b) show the profile of one of the contact bars. From these, one observes that the thickness of the heater is approximately 150 nm, which is a few per cent lower than the desired 155 nm that should have been deposited (5 nm Ti, 145 nm Cu and 5 nm Al). From these figures, one can also notice that the edges of all the profiles are higher than the rest of the heater, as marked in the figures. These reach as high as 175 nm. This might indicate skirts after lift-off but should not be a problem for the use as a heater.

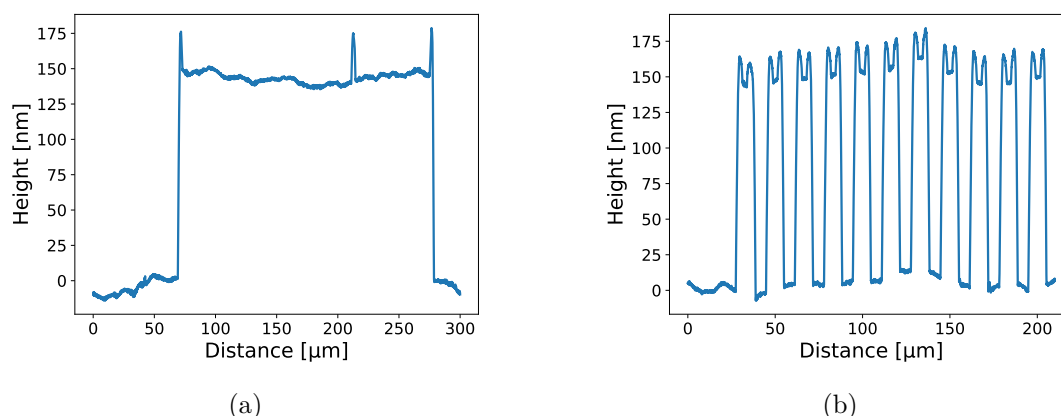


Figure 4.13: Profile measurements of the heating elements after fabrication, taken using a stylus profilometer. **a)** The profile across the long bar of the contact pad, the `lbar_w` parameter in figure 4.2 **b)** The profile of the main heating element. In both figures, unexpected increases in height is marked.

After fabrication of the heater on the 2-inch wafer, the sample was cut into 4.5×4.5 mm squares using a scribe before the chip was connected to an PCB and an LCC using a wire bonder. The results from this process can be seen in figure 4.14. Both images indicated proper bonding between the chip and carrier. Worth noting is that when performing wire bonding between the chip to the PCB, there were troubles due to the fact that the PCB was not flat. Several attempts had to be performed, and modification to the wire bonder stage was done before the final bonds were set. For this reason, there was some uncertainty in the quality of the bonds.

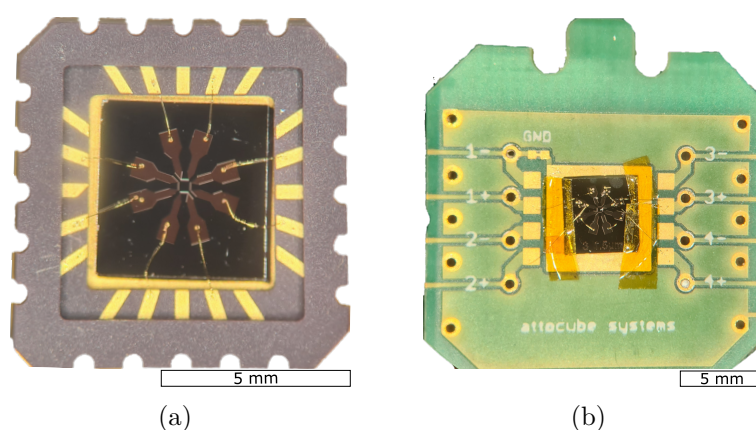


Figure 4.14: Images of the final device, where **a)** shows the chip attached to an LCC which is used in the three dimensional rotator (3DR), and **b)** the chip attached to a PCB which is used in the magnetic force microscopy (MFM).

4.2.2 Fabrication of micromagnets using optical lithography and metallisation

In order to characterise the properties of the heater, and explore if the heater works for its intended use, fabrication of micromagnets was attempted. SEM images of $\text{Ni}_{0.8}\text{Fe}_{0.2}$ micromagnets after fabrication using an optical lithography process followed by metallisation are displayed in figure 4.15. In figure 4.15(a) an array of these magnets, centred within the micro heaters, can be observed. The magnets have been centred properly and appear to be adequately defined. Further magnification of one magnet can be viewed in figure 4.15(b). The width and length of the magnet were measured in the SEM to be $1.12\ \mu\text{m} \times 8.85\ \mu\text{m}$, which is close to the desired $1\ \mu\text{m} \times 10\ \mu\text{m}$.

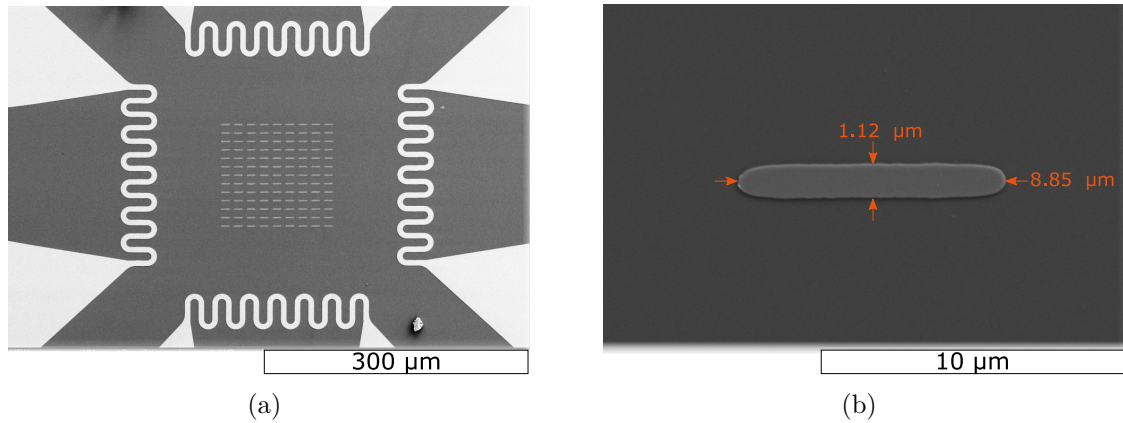


Figure 4.15: SEM Micrographs showing the fabricated microheaters. **a**) An array of micromagnets situated in the middle of the heating elements. **b**) Magnification of the image in **a**) showing a single micromagnet along with measurements of the dimensions. The dimensions are close to the desired value of $1\ \mu\text{m} \times 10\ \mu\text{m}$.

In order to test how the magnets respond to increased temperature, single domain magnets are sought after as one can measure if the temperature flips the magnetisation of the magnet. For this reason, the magnetic properties were measured using an MFM, and images of this evaluation are shown in figure 4.16. The measurements yielded minimal magnetic signal, but it appears as domain walls are present in the middle of the magnets. This is not ideal, as the magnets are not single-domain, and the proposed experiment cannot work as intended. However, the results are still fascinating, as the fabrication has shown that it is possible to create thin magnets using optical lithography, and it would be interesting to experiment on this in later research.

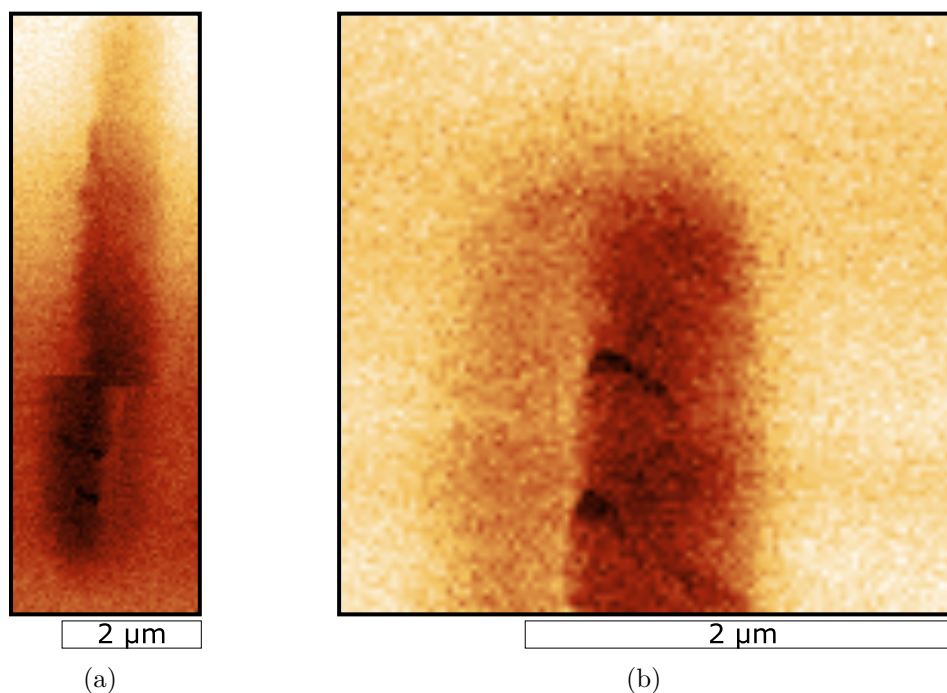


Figure 4.16: MFM measurements of the fabricated micromagnets. **a)** Magnetic measurements of the full magnets where the difference in contrast indicates difference in magnetic moment. From the images it appears as the magnet is not mono-domain, and a domain wall is present. **b)** A more accurate measurement of the upper part of the magnet in **a**. Here it is clear that there is a sudden shift in magnetic moment, indicating a domain wall is present.

4.2.3 Fabrication of nanomagnets using electron beam lithography and metallisation

As the micromagnets did not yield single domain structures, nanomagnets were fabricated. During this process, two different approaches to fabricate nanomagnets were performed. First, an attempt to fabricate nanomagnets on a chip already containing the micro heaters was pursued. Electron beam lithography (EBL) followed by metallisation was used for this process, and the result can be seen in figure 4.17. Above the number in this figure, there should be an array of nanomagnets, but as one can observe from the figure, there are no magnets to be found. This was an interesting result, as the lithography process used here has worked before. For that reason, a second identical process was performed, only this time on a clean wafer. The results of this trial can be seen in figure 4.18, showing that magnets have been fabricated.

Figure 4.18(a) show one of the arrays which had been fabricated in a square lattice formation, and a further magnification of this array is shown in figure 4.18(b). Measurements of these figures taken in the SEM indicated a size of approximately

185x75 nm. This is a bit smaller than the desired size but within an acceptable margin of error for this thesis. As the fabrication process of the nanomagnets yielded positive results, micro heaters were fabricated on the chip with the magnets, and thermal evaluation was conducted.

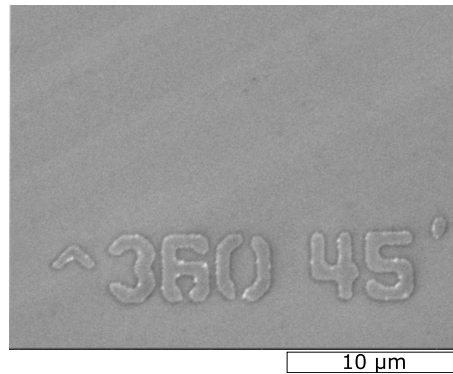


Figure 4.17: A SEM image of an area supposed to contain nano-magnets. The number indicates the lattice spacing and the angle of the magnets. Here it is clear that no magnets are present.

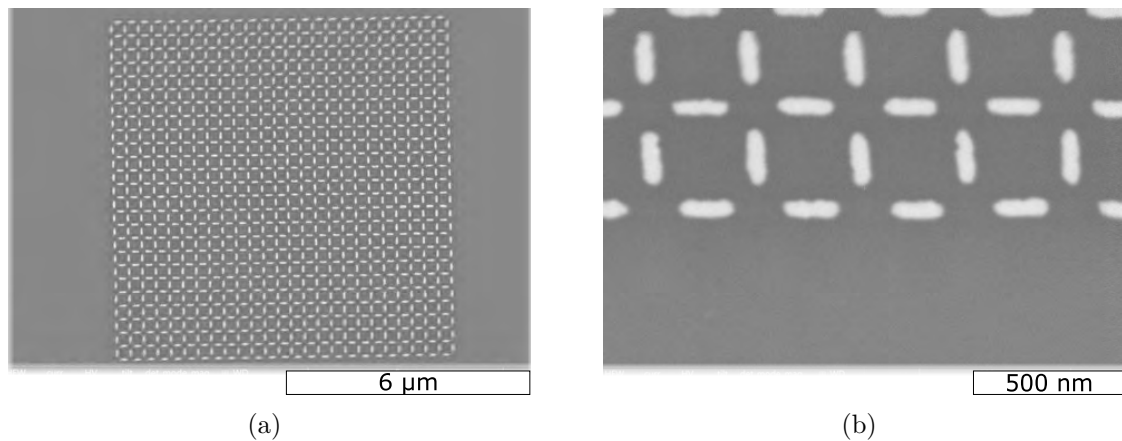


Figure 4.18: SEM micrographs of nanomagnets after fabrication. **a)** shows an array of magnets ordered in a square lattice formation. **b)** Magnified image of the magnets in **a**, showing properly fabricated magnet.

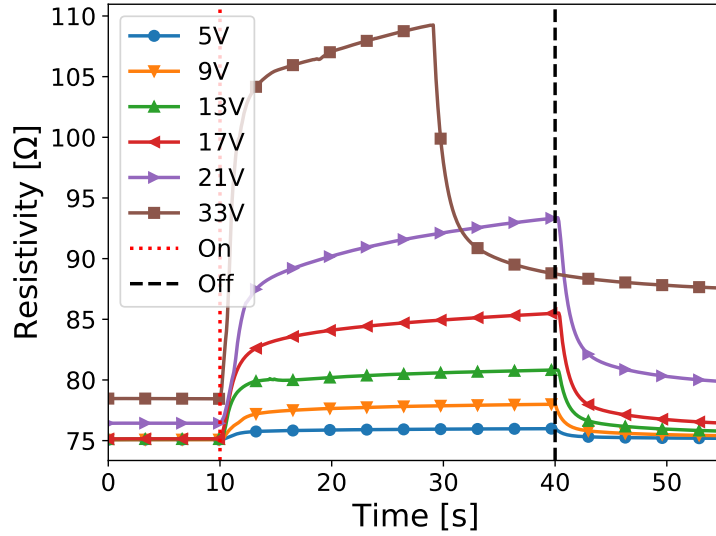
4.3 Characterisation of thermal properties of heater

After the heating elements and magnets had been properly fabricated, it was time to explore the thermal properties of the heater. First, the resistance of the heater was measured at room temperature. A resistance of $20.5 \pm 0.3 \Omega$ was measured across one heater, both before and after wire bonding, indicating that the bonds did not add any measurable resistance. One interesting observation is that the fabricated heaters have much higher resistance at room temperature than simulated using COMSOL. In figure 4.5, a resistance of 13.3Ω was measured at the beginning of the time evolution, and hence at room temp. The fabricated heating element will therefore have different thermal properties than in simulations.

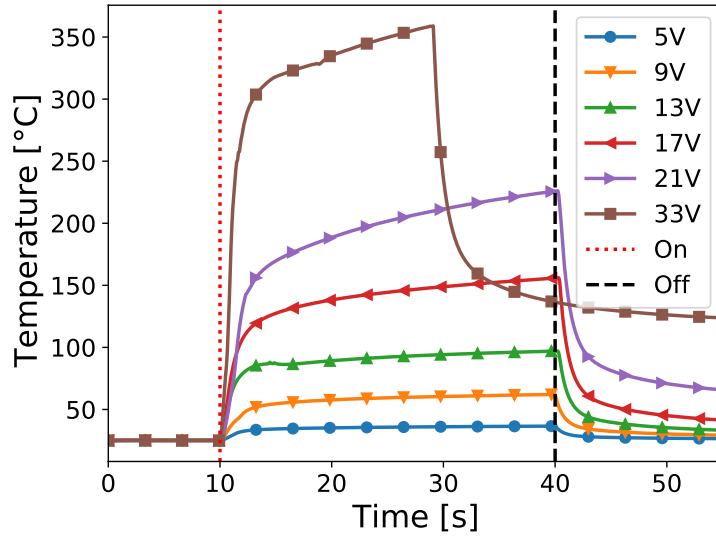
4.3.1 Thermal measurements of the heater

The first thermal measurements were performed using the LCC in the 3DR setup at room temperature. One heater worked as the heating element (C_h^{3DR} -circuit), while another worked as the measurement unit (C_m^{3DR} -circuit) as explained in figure 3.5(a). The first observations showed that the 3DR added an extra resistance 55Ω , further moving the system away from the simulations performed earlier. By applying a voltage ranging from 3 V to 33 V (C_h^{3DR} -circuit), yielded the resistance measurement in the C_h^{3DR} -circuit plotted in figure 4.19(a). Here, the resistance over time is plotted, and the moment the voltage is turned on is marked in the figure. Transforming these to a temperature using the temperature-dependent resistivity from equation (2.3), provides the plot shown in figure 4.19(b). It is assumed that the change in resistance happens within the heating elements and not in the rest of the setup. A temperature coefficient $\alpha = 0.00393$ was also used. The plots show an abrupt change in resistance as the power is turned on, indicating a fast change in temperature. Interesting to note is that at temperatures above 100°C , it appear as the temperature does not stabilise as it continues to increase, indicating that the system cannot remove the heat fast enough.

When applying a voltage of 33 V, which was the maximum voltage of the power source, the temperature increased rapidly above 300°C , and continue the increase until roughly 15 s after power on, before it drops. This indicates that the heating has stopped, which could mean that the heater is broken. Investigation of the heater afterwards, using optical microscopy, show that the gold wire had broken, which is shown in figure 4.20(a). In figure 4.20(b) images of the central heating element is shown, which also indicate that the heater has undergone some changes, most likely oxidation. Nevertheless, it seems like the limiting factor of the heater was the wire bond.



(a)



(b)

Figure 4.19: Plots showing the resistance measured and temperature calculated during thermal testing. Refer back to figure 3.5(a) for the circuit for the measurements, where $R_{3dr} = 55 \Omega$. **a)** The resistance measured over time in C_m^{3DR} -circuit for different voltages applied to the C_h^{3DR} -circuit. In the plot, the moment the voltage is turned on and off is also marked. **b)** Same plot as **a)** only the resistance is translated to temperature using (2.3) with a $\alpha = 0.00393$, $T_0 = 25^{\circ}\text{C}$ and $R_0 = 20.5 \Omega$. The load resistance $R_{3dr} = 55 \Omega$ is subtracted from the measured resistance before calculation.

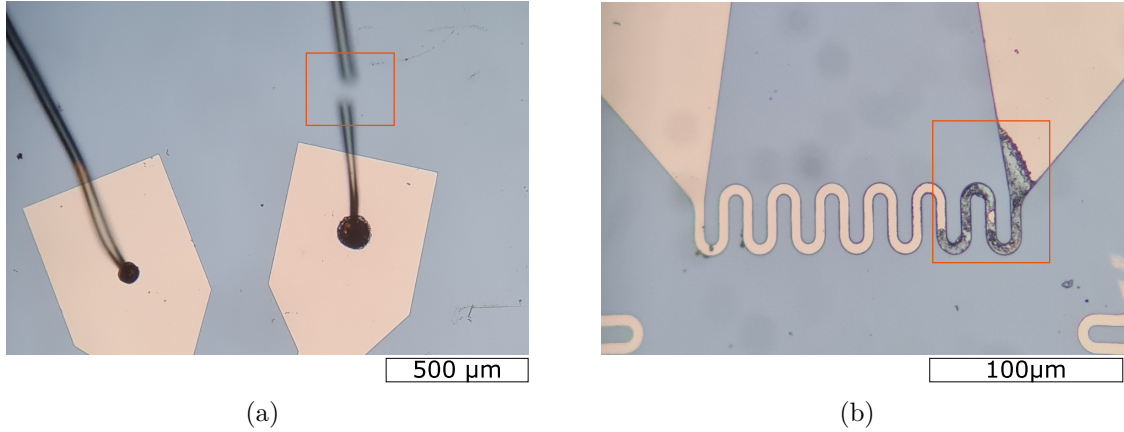
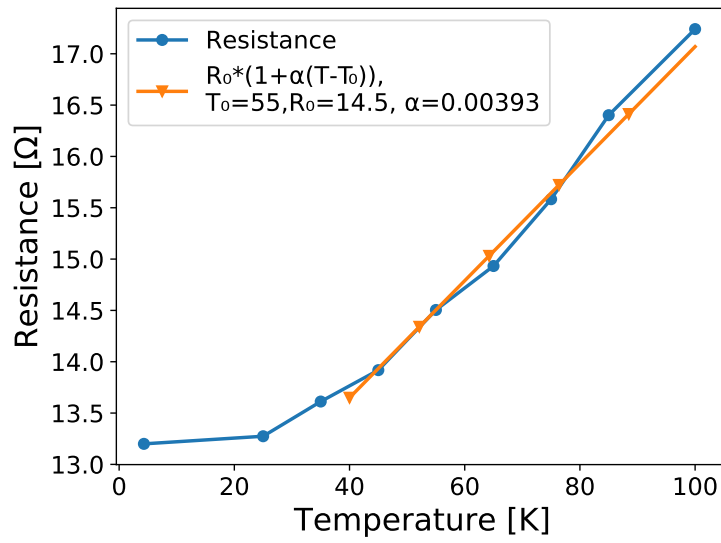


Figure 4.20: Optical images of the circuits after thermal measurements and a voltage of 33 V had been supplied to the circuit. **a)** A broken wire, as marked in the image, which caused the circuit to stop working **b)** The central heating element of the heater. Marked in the image is a that have been affected by the high temperature, most likely oxidation.

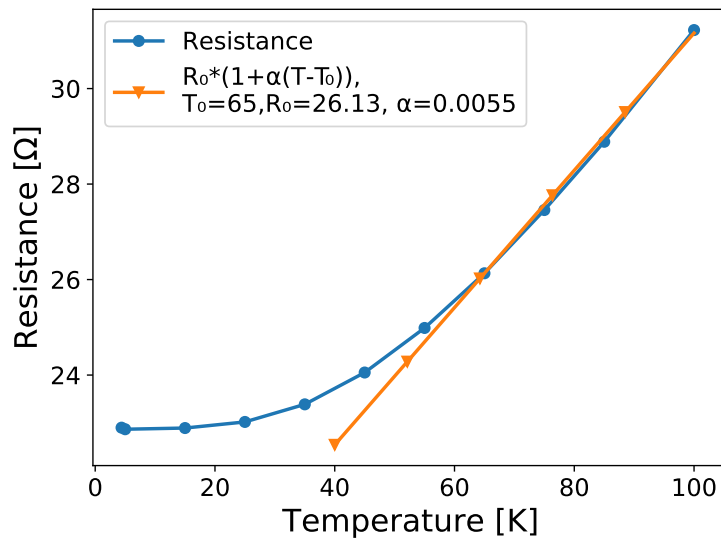
4.3.2 Magnetic force microscopy measurements of the nanomagnets

In order to observe if the heater works for its intended purpose, MFM measurements of the nanomagnets were performed after heating. The magnets and the heaters were cooled down to 4 K during these measurements to have a proper signal to noise ratio. Here, three heaters were connected in series to work as the heating elements, the C_h^{mfm} -circuit, while another, the C_m^{mfm} -circuit was used for measurements, as shown in figure 3.5(b). The added resistance from the MFM was much less than the 3DR, increasing the resistance of roughly $12\ \Omega$ at room temperature. For this setup measuring the load resistance at low temp was not performed as it would require to lower the temperature and measure the resistance without the heater connected. The fraction of load resistance to heater resistance of the total circuit is therefore not known.

Before any MFM measurements were taken, an attempt to calibrate the heater using the built-in heater of the MFM was performed. While increasing the temperature of the stage, and hence the heaters, the resistance of both circuits in figure 3.5(b) was measured. Plots of these measurements can be seen in figure 4.21. In figure 4.21(a), the resistance of the measurement circuit is plotted for different temperatures of the stage. Figure 4.21(a) show the resistance of the three heaters connected in series. When measuring the resistance of the single heater, high amounts of current was supplied from the source meter unit (SMU), and there were uneven measurements. Both plots do, however, show a resistance-temperature dependency that flattens out at low temperatures and become linear at around 50 K. For curiosity purposes, the temperature-dependent resistivity from equation (2.3) is fitted to the linear part of



(a)



(b)

Figure 4.21: Resistance measurements during calibration in the MFM, where a temperature is applied to the circuit from the built stage heater. Refer back to figure 3.5(b) for the circuit diagrams. Note, that these measurement uses both circuits for measuring the resistance. **a** Resistance in the stand-alone heater, the C_m^{mfm} -circuit from figure 3.5(b), for different temperatures supplied by the stage heater. **b** Resistance in three heaters connected in series, the C_h^{mfm} -circuit as shown in figure 3.5(b), for different temperatures applied from the stage heater. Both plots have been fitted with equation (2.3), at the point where they start to become linear, calculating an $\alpha \approx 0,0055$ for **a** and $\alpha \approx 0,0055$ for **b**.

the curve in both plots, giving two different temperature coefficients.

After applying some current to the C_m^{mfm} -circuit, although unclear how much, it broke, and a resistance of $16.6 \text{ k}\Omega$ at 4 K was measured. Interestingly, further inspection after MFM measurements showed a resistance of 0.242Ω at room temperature, indicating that the resistance decreases with higher temperature. Optical images of the circuit, displayed in figure 4.22 further indicated that there were some abnormalities in the contact region. Nevertheless, as the resistance changes with temperature, it could still be used to indicate how the temperature of the system changes with increasing voltages.

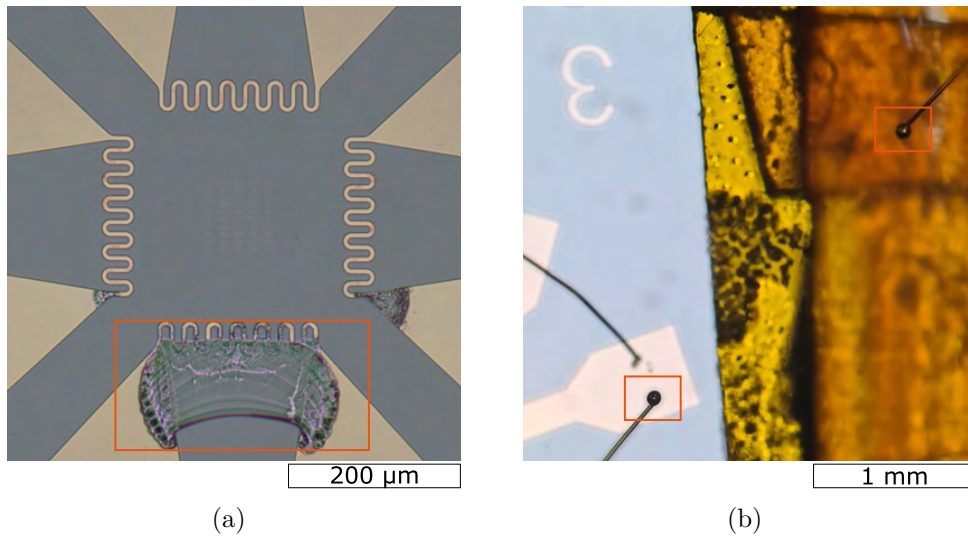


Figure 4.22: Optical images of the circuits after magnetic measurements. **a)** Shows the measurement circuit that broke during calibration, indicating some sort of contact formed across the silicon substrate as marked on the image. **b)** The broken wire after heat had been supplied to the system. Both parts of the wire are marked on the image, showing that a gold ball has formed on both wires indicating melting and high temperatures.

For the magnetic measurements, the magnets were first initialised in one direction using a magnetic saturation field $M_s = -0.1 \text{ T}$ and applied a positive bias field B_{bia} as explained figure 3.6. MFM-measurements of this experiment are shown in figure 4.23. The white contrast indicates a negative magnetic field, while the black contrast indicates a positive as compared to the magnetisation of the tip of the MFM. As one can see in figure 4.23(a)-4.23(d) all magnets point in the same direction. From this, it is clear that applying a positive bias of 0 mT to 45 mT does not carry enough energy to flip the magnets. However, in figure 4.23(e) a bias field of 50 mT was applied, and the measurements showed that the magnetisation of some magnets had flipped. One can from that stipulated that this is approximately the field required to flip the magnetisation.

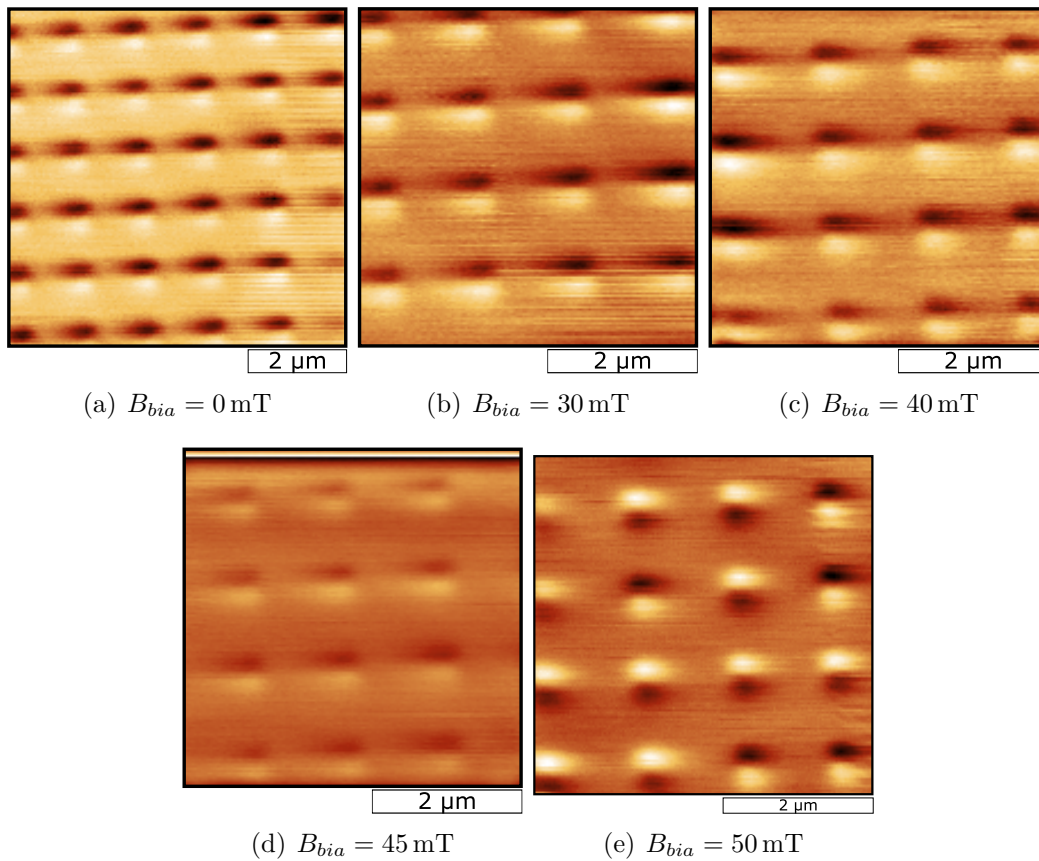


Figure 4.23: MFM images of nanomagnets first initialized with a magnetic field of -0.1 T , and then applied a bias field in the other direction using a magnetic field of B_{bia} as explained in figure 3.6. Here white contrast indicates a negative pole, while black indicates a positive with respect to the magnetisation of the tip. From figure **a-d**), where bias field of 0 mT to 45 mT are applied, none of the magnets have reversed its magnetisation, indicating the bias field is lower than the coercive field. In **e**) some magnets has reversed their magnetisation indicating the coercive field on the level of roughly 50 mT .

After measurement on how the system responds to a bias field without temperature had been conducted, the magnets were saturated again using the same saturation field. A voltage was then applied to the C_m^{mfm} -circuit at the same time as the bias field, and new measurements were conducted. Results from these evaluations are shown in figures 4.24 to 4.27.

The magnets was first initialised with the white contrast pointing down, as shown in figure 4.23. From figure 4.24 one can see that at $B_{bia} = 50$ mT all the magnets flip while applying 3 V to the C_m^{mfm} -circuit. This indicated small amounts of energy is necessary to flip the magnets. Decreasing B_{bia} also means that the system needs more energy to flip, and in figure ref 4.25 and 4.26 it is shown that for a B_{bia} of 45 and 40 mT all the magnets have flipped when applying a voltage of 4 V and 7 V to the circuit.

For $B_{bia} = 30$ mT, which is shown in figure 4.27 a voltage of 17 V is needed before most of the magnets flip. However, there are still some magnets that did not flip, indicating higher voltage/temperatures were necessary. Here, it is worth noting that when applying 17 V, the entire chip shifted position on the stage of tens of micrometres, and a new area to evaluate was therefore found. This is the reason the field of view looks a bit different.

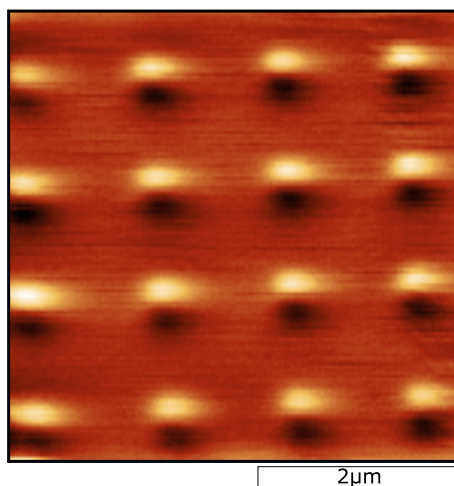


Figure 4.24: MFM measurements of nanomagnets that have been initialized with a magnetic field of -0.1 T facing all the magnets south (black contrast up), and applied a bias field of $B_{bia} = 50$ mT as well as heated by the micro heater using a voltage of 3 V. The measurements indicate that a voltage of 3 V or less is needed to flip all the magnets.

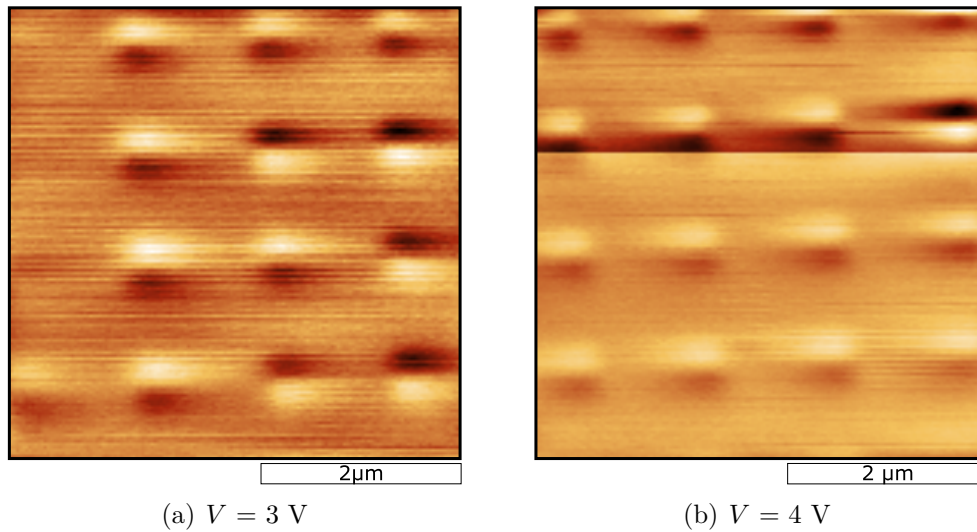


Figure 4.25: Images from MFM measurements of nanomagnets that have been initialized with a magnetic field of -0.1 T facing all the magnets south (black contrast up), and applied a bias field of $B_{bia} = 45$ mT as well as heated by the micro heater using a voltage of **a)** 4 V and **b)** 5 V. The measurements indicate that a voltage of roughly 4 V is needed to flip reduce the coercive field to roughly 0.45 mT.

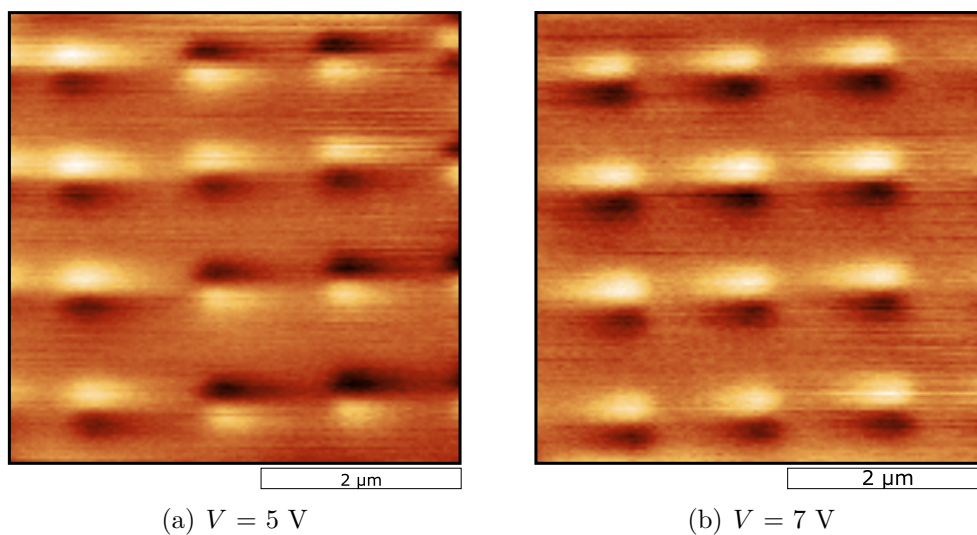


Figure 4.26: MFM measurements of nanomagnets that have been initialized with a magnetic field of -0.1 T facing all the magnets south (black contrast up), and applied a bias field of $B_{bia} = 40$ mT as well as heated by the micro heater using a voltage of **a)** 5 V and **b)** 7 V. The measurements indicate that a voltage of roughly 7 V is needed to flip the magnetization.

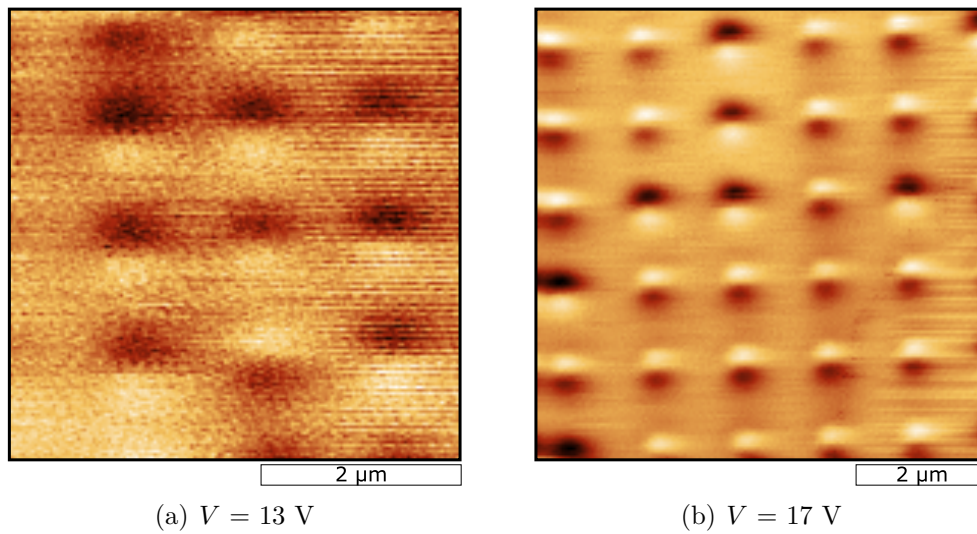


Figure 4.27: MFM measurements of nanomagnets that have been initialized with a magnetic field of -0.1 T facing all the magnets south (black contrast down), and applied a bias field of $B_{bia} = 30 \text{ mT}$ as well as heated by the micro heater using a voltage of **a)** 13 V and **b)** 17 V . The measurements indicate that a voltage of above 17 V is needed to flip the magnets, as there are still a few magnets pointing north.

The last measurement performed was without a bias field to observe if the heater could flip the magnetisation of the magnets independently of any magnetic field. Again, the magnets had been initialised with white contrast pointing down, as viewed from the paper plane. The maximum voltage of the power source, 33 V , was applied to the heaters, and the MFM measurements performed afterwards can be viewed in figure 4.28. Once again, the chip shifted position after heating had been performed. From the figure, one can observe that thermal activation has occurred, and approximately 24.5% of the magnets have flipped. However, after these measurements, it was not possible to supply any current to the circuit, and therefore, repeated measurements could not be performed. After inspecting the heaters under an optical microscope, one can once again observe that the wire had broken, creating an open circuit, as seen in figure 4.22(b).

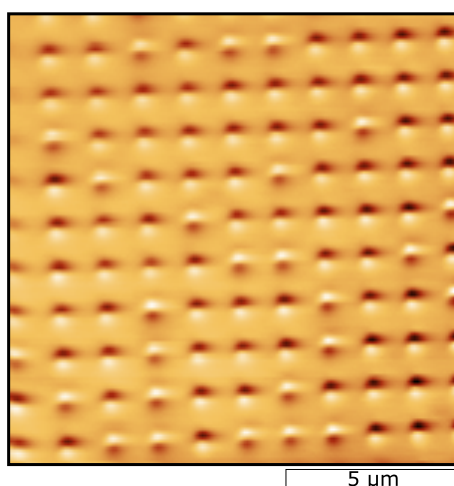


Figure 4.28: MFM images taken after nanomagnets were initialised using a magnetic field of -0.1 T. The magnets were then heated using the microheaters by applying an increasing voltage of 0 V to 33 V over approximately 30 s and using no external magnetic field. Of the approximate 106 visible magnets, 26 of them changed magnetisation, indicating that there has been thermal activation, and the thermal energy is on par with the energy of the coercive field.

During these evaluations, the resistance of the C_m^{mfm} -the circuit was recorded and can be observed from the plot in figure 4.29. The temperature dependency of the resistance appears to have reversed as an increasing voltage/temperature decreases the resistance. The resistance at room temperature was also measured, showing resistance of 242Ω , this is also showed in figure 4.29. From the plots, one can also observe that the resistance of the circuit at 17 V is approximately the same as the resistance measured at room temperature. Indicating that the temperature of the measurement heater, and thus, the temperature of the magnets, reached room temperature at this voltage. Furthermore, at 33 V the resistance is about half that of room temperature, indicating a temperature well above room temperature, but it is unclear by how much.

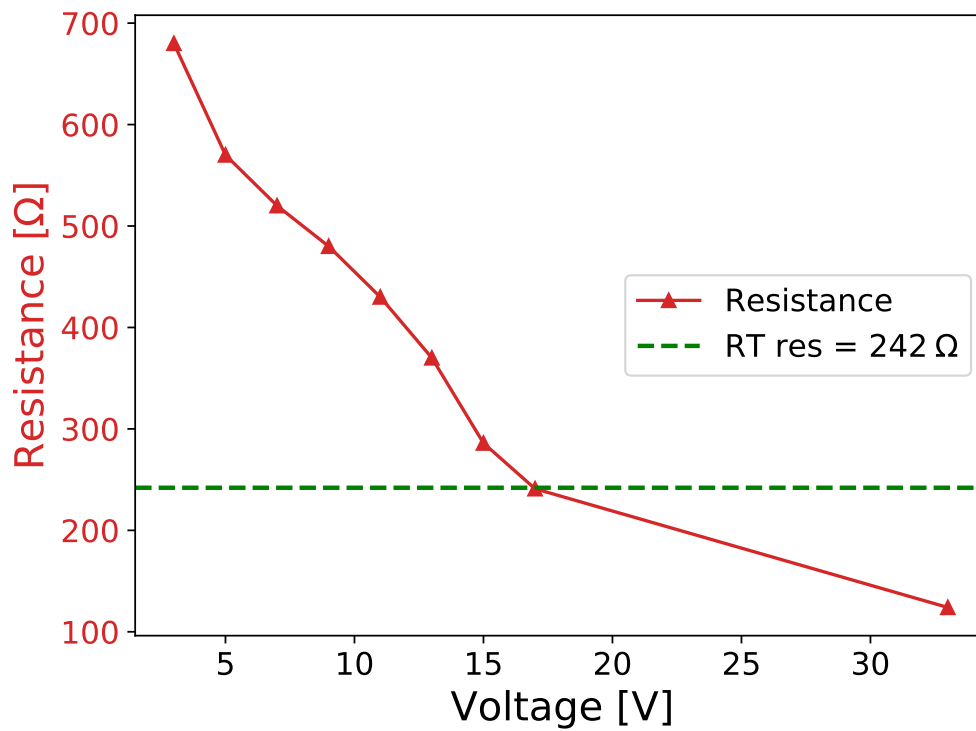


Figure 4.29: Plots showing the resistance measurements of the C_m^{mfm} -circuit during magnetic evaluation. Here the resistance is shown for different voltages. The measurement heater changed during calibration, and a decreased resistance is measured as the temperature/voltages increases. The resistance measured at room temperature after the magnetic evaluations is also shown, indicating that a voltage of 17 V increased the temperature of the system by roughly 300 K.

5 | Discussion

In this chapter, the results presented in chapter 4 will be evaluated and discussed in the same order as in previous sections. First, results from the simulations will be discussed, followed by the fabrication and ending with the thermal properties of the heater. Although the discussion will mostly follow this order, aspects from the different sections are relevant to discuss concurrently and will be done so.

5.1 Simulations

The simulations quickly showed that the design implemented yielded satisfactory results compared to the properties first envisioned in the introduction. From figure 4.4 it was shown that an acceptable temperature in the area of interest, the area of interest (AHA), was achieved. Furthermore, the temperature stabilised relatively quick, as seen from the time simulations in figure 4.5 and 4.6. Well within the desired time of 2s. As the design was fully parameterisable, it was possible to evaluate different dimensions of the heater, to optimise the thermal properties. From these simulations, no unusual results were found. The temperature and current changed as one would expect from the theory of resistivity (2.2) and Joule's law (2.1), but it did allow for envisioning the exact temperature and current the whole system would achieve. A system that, in an ideal world, should yield the desired temperature was found by fine-tuning the parameters.

For these simulations, a constant voltage was applied to the system. Ideally, if a specific current limits the lab system, it would be beneficial to apply a constant current instead of voltage during simulations. However, one must consider thermal runaway. As the resistance increases with temperature, the thermal power will continue to increase, making the simulations impossible to solve and the lab system to break. Nevertheless, it could prove valuable for measuring the limits of the system.

After initial testing of the design had been performed, it became clear that it did possess the functionality intended. Ideally, it would be beneficial to have simulations that imitate the exact setup found in a lab environment. However, as there were

many variables to consider, some simplifications had to be done. In this system, one large simplification relating to heat transfer by conduction was used. A constant temperature was applied to the edges of the system, allowing for conduction through those areas, dissipating heat. Nevertheless, the printed circuit board (PCB) and leadless chip carrier (LCC) used in experiments are made up of plastic parts that do not conduct heat efficiently. As mentioned in chapter 2, plastic, or low-density polyethylene (LDPE) have a coefficient of thermal conduction of about 0.33 W/mK , compared to 385 W/mK for copper or 150 W/mK for Silicon. For the simulations, plastic domains were not added to the system, as it would increase the system's complexity, increasing both time and memory usage.

To limit the difference of conduction in experiments and simulations, conduction was applied to the edges of the chip instead of the backside. In experiments, the chip was connected through the backside, and therefore this was the area conduction should take place in simulations. However, as conduction directly relates to the area of contact, one can limit the amount of conduction by applying it to a smaller area. Nevertheless, it was clear that these simplifications limit the accuracy of the simulations, and improvements should be made. One could, for instance, conduct experiments on the experimental setup measuring the conduction parameters of the system. This could then be used in simulations by adding a temperature-dependent heat flux to the simulations, mimicking the system in the lab.

The design chosen in this thesis consisted of four heaters, which all could work as separate heating elements. There are several other designs that could have been implemented, for instance, the one used by Xu et al. and Morley et al. [43, 44], where several windings of Pt was used for the heater. However, the design in this thesis was created for its capability of generating a temperature gradient across the spin ice structures, as it could be interesting to observe how artificial spin ice (ASI)-structures experience different temperatures within the system. Although this has not been tested in a lab environment due to the lack of an accurate measurement system, initial simulations indicate that this was possible. These can be seen in the appendix B, showing a temperature difference of roughly 40 K , through the AHA.

Simulating the system proved valuable, as one could predict, to a certain extent, how the system behaved. After simulating the design, it was also beneficial that it could easily be exported to a file format suitable for lithography, thereby allowing for the fabrication of the same design as simulated.

5.2 Fabrication process

Throughout the lithography process, both a negative and positive photoresist was evaluated. The goal of this process was to arrive at a versatile procedure capable of achieving structures with arbitrary line widths, both in order to fabricate heaters

of different dimensions, as well as creating micromagnets. From the dose and development results in figure 4.11, it was clear that using SPR700 with the parameters given in table 4.2 yielded acceptable results. However, the choice to discard ma-N 440 occurred relatively early during this thesis, as there were problems of consistency during development. After discussing with the engineers at NanoLab, it was found that there had been several problems with the developer in question, and this had been solved later on. Further testing using ma-N 440 could therefore be considered if undercut is desirable. With the time available for this thesis, it was not investigated further.

Inspecting the heaters after fabrication yielded some interesting result. Although the lateral dimensions of the heater showed more than satisfactory, the height profile of the heater was unexpected. The edges of the heater were several nanometres higher than the rest of the sample, as shown marked in figure 4.13. Although this should not be relevant for the final characteristics of the heaters, it indicates where the limitations of the formulated process can occur. The reason for these high edges was, most likely, deposition of metal along the sidewalls of the resist. After lift-off, some of the metal on the walls will remain on the sample, leaving higher edges. It could be beneficial to use a negative resist with an undercut profile to avoid this. It is, however, easier to achieve higher resolution using the positive resist and therefore, one should weigh the pros and cons of each process individually [45]. For the purposes of the work in this thesis, a positive resist was deemed the better option, as the edges should not cause any problems for the final heater.

The fabrication of micromagnets further showed the versatility of the lithography process. The dose and development test indicated that structures with dimensions of $2\ \mu\text{m}$ could be created, while $1\ \mu\text{m}$ structures could prove difficult. However, the micromagnets were fabricated with a width of $1.12\ \mu\text{m}$ showing that it was possible to reach dimensions close to $1\ \mu\text{m}$. This is interesting results as the lowest feature size of the MLA150 is $1\ \mu\text{m}$ [46]. As there are several parameters affecting the lithography process, such as the cleanliness of the sample, the type of resist and developer resist and developer it is not easy to achieve the optimal line width the MLA150 can produce. For that reason, the lithography process has been deemed highly successful [34].

The micromagnets did, however, not appear to be single domain as shown in figure 4.16. Some initial micromagnetic simulations were performed by PhD candidate Anders Strømberg using the MuMax³ simulator [47], which showed that $2\ \mu\text{m} \times 10\ \mu\text{m}$ magnets could form as single-domain. These simulations are shown in appendix A. Furthermore, in an article by Imre et al. from 2006, permalloy magnets having different aspect ratios was evaluated; here, they show that a $0.85\ \mu\text{m} \times 3\ \mu\text{m}$ magnet yields single-domain results while a magnet with $1.1\ \mu\text{m} \times 3\ \mu\text{m}$ dimensions does not [48]. It could indicate that the micromagnets fabricated during this thesis are close to being single domain. Further investigations, especially by fabricating smaller

magnets, and testing different aspect ratios, could help to achieve single-domain magnets. Creating these magnets using optical lithography could be beneficial for testing purposes as it is a much faster and easier process than using the Electron beam lithography (EBL).

The first attempt of fabricating nanomagnets proved unsuccessful, as shown in figure 4.17. The process used for the fabrication was well known to work within the group, and therefore these were interesting results. It is believed that the unsuccessful fabrication was due to performing lithography on a sample already containing micro heaters. When performing spin-coating, the resist would not distribute evenly as large structures impede the flow. Hence, during exposure, the correct thicknesses were not used when calculating the exposure dose. There were two possibilities of circumventing the problem: using a higher dose, which would mean the need for a new optimisation process or fabricating the heater after the magnets. The last was performed during this thesis and proved successful. It is noted that for later fabrication, the heaters should be fabricated after the nanomagnets.

5.3 Thermal characterisation

The heaters initial resistance measurements showed a large difference in resistance between the fabricated heater and the one used simulations. A resistance of $13.2\ \Omega$ was calculated in simulations compared to a resistance of $20.5\ \Omega$ in the fabricated heaters. Several factors could explain this difference. First, and maybe the most apparent, is the use of bulk resistivity of copper in simulations. Khojier and Savaloni showed in a paper from 2013 that thin films of copper reach bulk resistivity at approximately 160 nm [49]. In the fabrication process, 145 nm of copper was deposited, and from profile measurements shown in 4.13(b), it appears as part of the heater was thinner than this as well. For the simulations, a resistivity of $1.71 \times 10^{-8}\ \Omega\text{ m}$ while in the article above indicated a resistivity of roughly $1.8 \times 10^{-8}\ \Omega\text{ m}$ at 140 nm. Therefore this can account for some of the increased resistance, but not all. Other effects such as impurities introduced in the deposition process might affect the results, but further investigation should be done. For instance, one can test different resistivity values in simulations or change the deposition rate during evaporation of the physical heaters.

5.3.1 Heating properties

From resistance measurements using the three dimensional rotator (3DR)-system as presented in figure 4.19(a), an increased resistance was measured, which in turn indicate an increased temperature. From figure 4.19(b), where the increased resistance had been translated to temperature, it was found that applying a voltage of 13 V to a single heater would increase the temperature of the other by 100 °C. Furthermore,

the resistance appears stable at this voltage/temperature, indicating that the system manages to dissipate heat fast enough for a stabilisation in temperature to occur. There are, however, some assumption that needs to be addressed. In this instance, it has been assumed that the only change in resistance occurs in the heater and not in the load resistance. Although this is a fair assumption, as the system is vast compared to the heater, and heating should only happen locally, other parts of the system can be affected. The temperature coefficient of resistivity used is also only valid at room temperature, which would affect calculation at higher temperatures. Nevertheless, one can assume that these numbers are close to the actual temperature.

From the measurements, one also observes that stabilisation in resistance only occurs at lower voltages, indicating that the thermal power is higher than what the system can dissipate at a higher voltage. The fact that the end temperature is not the same as the starting temperature also indicates that heat is trapped somewhere in the system and cannot dissipate fast enough for the system to re-stabilise. A cooling spray was used in these tests to reduce the temperature back before trying the new voltage. When doing this, it was noted that it does take some time, more than thirty seconds, to reduce the temperature back again. Where the heat is trapped is hard to tell, but there are plastic parts within the PCB and the instrument as well as open spaces around the chip that cold trap the heat. Nevertheless, the plots show that it is possible to heat the sample to a temperature of 100 °C, relatively fast.

Further analysing the plots, one can deduce the time to increase and decrease the temperature. Here it has been chosen to observe the time for increasing the temperature to 80 % of its maximum value, as well as the time for decreasing it to 20 % above the minimal value. These values can be seen in table 5.1. Looking at the time to increase the temperature, one can observe that the time is longer than in simulations. This further indicates poor heat transfer. If the system cannot dissipate heat fast enough, it will stabilise at a higher temperature which takes longer. Nevertheless, this also means less power is necessary to reach a high temperature, and as these number similar to what was desired at the beginning of this thesis, the heaters can be deemed successful.

5.3.2 MFM measurements

In the last part of this thesis, magnetic measurements were performed, which further proved the thermal properties of the heater. As explained in chapter 3, a calibration of the heaters was first attempted. These result, which is supplied as plots in 4.21, shows how at low temperatures, the resistance stabilises at temperatures close to absolute zero; which is as expected from the theory of resistivity. However, the resistivity measurements of the single heater were unstable, which is believed to be due to the high current supplied from the Ohmmeter during measurements. A current of 100 mA was supplied, which is a current high enough for a high amount of

Table 5.1: Time to increase the temperature to 80 % of max value and decrease it again from max, to 20 % of the end value for different voltages

Voltage [V]	Increasing temperature[s]	Decreasing temperature[s]
5	0.83	0.74
9	2.31	2.56
13	1.74	4.79
17	4.38	6.69
21	7.60	6.69
33	2.31	7.36

heat to be generated. This may have affected the measurements. The source meter unit (SMU) did not allow for the current to be changed as the resistance was too low, and another method of measuring the resistance should therefore be considered for better calibration.

Furthermore, after applying current to the single heater, it broke; it is unclear why, as the current supplied was roughly 300 mA, a current the heater should withstand. Nevertheless, the state of the circuit after it had broken yielded some fascinating results. A resistance of 16.5 k Ω was measured in the heater, and heat supplied to the system caused the resistance to decrease. For metals, the resistance should increase with temperature, indicating that something else is present. Further investigations using the optical microscope shows that there are deformations in the heater, as marked in figure 4.22(a). Both these findings lead to the conclusion that the current has to move through the silicon substrate as the conductivity of semiconductors increases with temperature. Although the broken measurement heater limited the possibility of using it as an accurate "thermometer", the resistance still changed with temperature, providing some information regarding the temperature of the system.

Although resistance in the circuit changed with temperature, as proven by the decreased resistance at room temperature, a voltage was supplied to the other circuit in the system. This voltage could also increase the conductivity of the silicon substrate. Therefore, it was not known how much the different aspects affected the system, and if it had been time, further analysis should have been performed.

A summary of the magnetic force microscopy (MFM) measurements presented in chapter 4 is given in figure 5.1. One can observe that a higher voltage/temperature is needed to flip the magnetisation of the magnets, as a lower bias field is applied to the system, proving how the heater affects the coercivity of the system. When comparing the resistance of the heater during these evaluations to the resistance measured at room temperature, as done in figure 4.29, it could appear that at 17 V the system

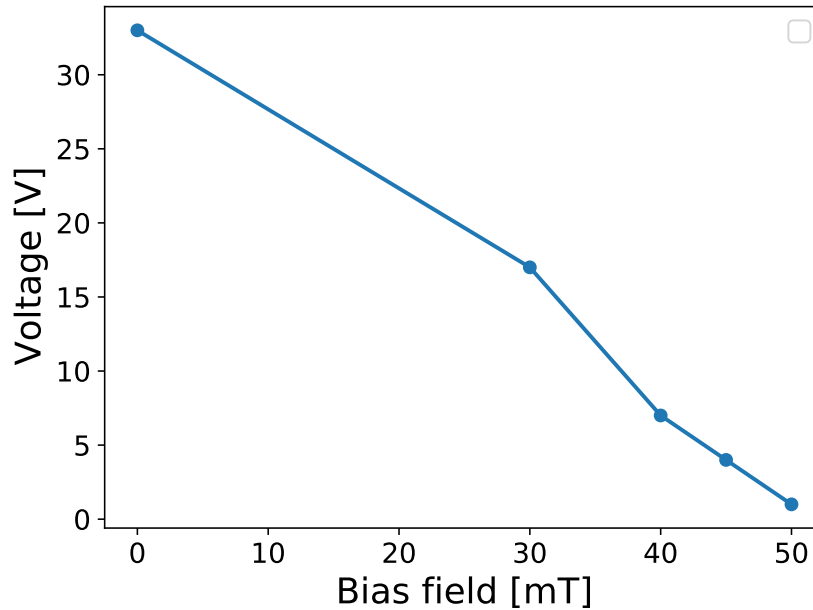


Figure 5.1: A summary of the MFM measurements given in chapter 4 indicating at what voltage all, or most, of the magnets had been thermally activated. Here one observes that the voltage needed to flip the magnets decreases with an increasing bias field, indicating the voltage applied gives energy to the system.

reached room temperature. This indicates that the circuit provided an increase in temperature of almost 300 K. Furthermore, The much lower resistance at 33 V, and ability to flip unbiased magnets, indicates that the local temperature is well above room temperature, although difficult to determine exactly how much. However, as mentioned, these resistance measurements are uncertain, and the temperature may be lower.

When 17 V and 33 V were applied to the system, there was a sudden shift in the placement of the substrate, and it became more difficult to perform MFM-measurements. This shift can be due to thermal expansions in the copper tape, which was used to attach the chip to the PCB. Other explanations may be that the adhesion was not good enough, and large changes in temperature may have moved the sample. One way to improve this would be to use glue instead of copper tape for attachment. For instance, silver epoxy could be used, still keeping the thermal properties needed for conduction but also having better adhesion.

A limiting factor of the circuit has proven to be the wire bonds. Both in temperature measurements, as well as during magnetic measurements, the wire broke during heating, as can be seen from figure 4.20(a) and figure 4.22(b). The wire had a diameter of 25 μm and therefore a cross-sectional area much larger than the heater;

it should therefore not be any heating produced by the gold wire. However, if stress had been introduced in the wire during wire bonding, weak parts much smaller than the diameter of the rest of the wire may have been present. This can, at high currents, cause high local heating and melting of the wires. Several bonds can be made between the contact pad and the PCB/LCC to remove or at least reduce this effect.

6 | Conclusion

In the course of this thesis, a design capable of thermally activate artificial spin ice systems have been created, simulated and physically realised in the laboratory. A design consisting of four separate heating elements was devised and then simulated using COMSOL Multiphysics. In the simulation, different aspects of the heater were tested to arrive at the optimal system capable of delivering a temperature of 100 °C. Here, the system was both simulated to observe how the heat diffuse through the system and observe how long it takes for the temperature to stabilise. It was found that the temperature within the area of interest (AHA) is relatively uniform and stabilises after roughly 50 ms. Nevertheless, there were shortcomings in the simulations, especially in how heat conduction is added to the system, as it does not mimic how the lab setup works. The heat conduction is much higher than what is observed in a physical system, and further improvements should be conducted.

Furthermore, the device was physically realised through lithographic fabrication by metallisation. Testing was performed to arrive at a versatile fabrication process capable of achieving line widths in the design close to 1 μm . Although not done in this thesis, this allows for experimentation of heaters of different dimensions. If combined with simulations, this can optimise heaters with the properties desired for a given system. Additionally, the versatility of the process allowed for the fabrication of micro-magnets, which, although did not appear being single domain, could be an exciting topic for further experimentation.

The thermal properties of the heater were measured in the end. Here, by measuring the resistance during heating, a stable temperature of 100 °C could easily be achieved by applying a voltage of 13 V to a single heater. Although these measurements cannot determine the exact temperature, due to uncertainties in the measurements, there is no reason to believe the measured values were far from the actual temperature. Moreover, the thermal properties were characterised by measuring the change in coercivity of nanomagnets as heat was supplied to the system. These measurements further support the evidence from the resistance measurements, as they show an increase of temperature well above 100 °C

6.1 Further Work

The time of this thesis did not allow for accurate testing on how the heaters affect artificial spin ice (ASI)-systems. Therefore, one obvious route for further examination would be to use the heaters for what they are intended. Furthermore, it could be interesting to attempt to apply a heat gradient across the system, as the designed heater should allow for it.

The calibration and temperatures measurements used in this thesis has shown their shortcomings, and better methods should be formulated for measuring the exact temperature of the system. A four-point probe measurement system could be implemented as it could remove the load and contact resistance from the circuit [50]. This does, however, mean that more contacts have to be formed, which might impede the design. Other techniques that have been considered in this thesis, but time and equipment did not allow for, are pyrometric measurements or temperature measurements using Raman microscopy [51]. Both of these could potentially also show the temperature gradient across the system, which would be interesting.

As mentioned before, in order to have more accurate simulations, the heat transfer module of the simulations should be further investigated. Even though having simulations that completely describes a given system is impossible, it can be improved. For instance, conducting experiments on heat transfer in the lab can be performed, and then the measured heat flux can be added to the system. Also, it is possible to increase the system's complexity by, for instance, adding plastic to it. This can further improve the simulations.

To summarise, a versatile process capable of both simulating and fabricating micro-heaters has been achieved. In-addition, these heater has proven capable of thermal activation of nanomagnets, and could therefore be used in further research on ASI-systems. However, some improvements can be made, such as higher complexity simulations and better measurement techniques.

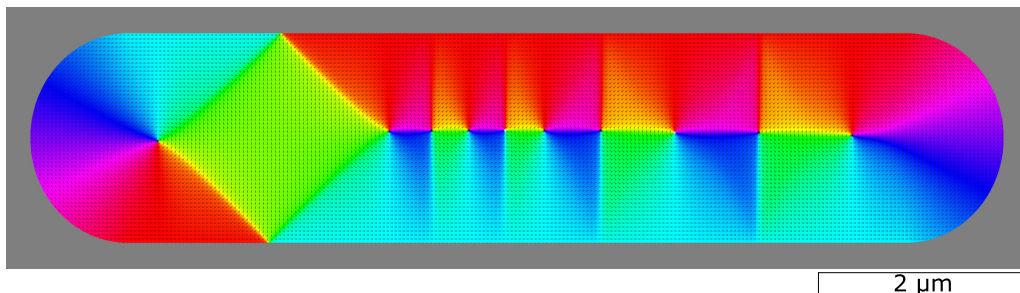
References

- [1] Waldrop, M. M. (2016). “The chips are down for Moore’s law”. *Nature* 530 (144–147).
- [2] Meyers, R. A., ed. (2009). *Encyclopedia of Complexity and Systems Science*. Springer New York.
- [3] Jensen, J. H., Folven, E., and Tufte, G. (2018). “Computation in artificial spin ice”. *The 2018 Conference on Artificial Life*. MIT Press.
- [4] Hon, K. et al. (2021). “Numerical simulation of artificial spin ice for reservoir computing”. *Applied Physics Express* 14 (3) 033001.
- [5] Hadaeghi, F. (2020). *Neuromorphic Electronic Systems for Reservoir Computing*. arXiv: 1908.09572 [cs.ET].
- [6] Skjærvø, S. H. et al. (2019). “Advances in artificial spin ice”. *Nature Reviews Physics* 2 (1) 13–28.
- [7] Jain, A. and Goodson, K. E. (2011). “Thermal microdevices for biological and biomedical applications”. *Journal of Thermal Biology* 36 (4) 209–218.
- [8] Lee, D.-W. and Oh, I.-K. (2007). “Micro/nano-heater integrated cantilevers for micro/nano-lithography applications”. *Microelectronic Engineering* 84 (5-8) 1041–1044.
- [9] Chodos, A. (2009). “December 1840: Joule’s abstract on converting mechanical power into heat”. *APS physics* 8.
- [10] Young, H. and Freedman, R. (2011a). *Sears and Zemansky’s university Physics with Modern Physics, chapter 25*. 13th. Pearson Education 818–850.
- [11] Kittel, C. (2005). *Introduction to solid state physics*. Hoboken, NJ: Wiley.
- [12] circuits, A. about (n.d.). *Temperature Coefficient of Resistance*. accessed: 08.06.2021.
- [13] Callister, W. (2010). *Materials science and engineering : an introduction*. Hoboken, NJ: John Wiley & Sons.
- [14] Young, H. and Freedman, R. (2011b). *Sears and Zemansky’s university Physics with Modern Physics, chapter 17-20*. 13th. Pearson Education 551–686.
- [15] Ziabari, A., Bian, Z., and Shakouri, A. (2021). “Adaptive Power Blurring Techniques to Calculate IC Temperature Profile under Large Temperature Variations”.

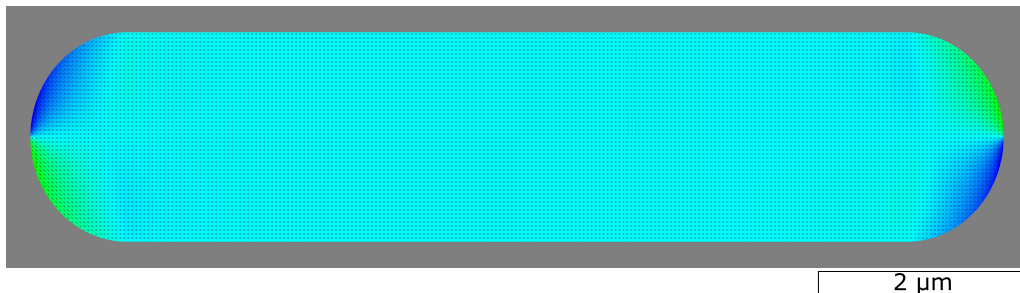
- [16] Thompson, J. and Younglove, B. (1961). “Thermal conductivity of silicon at low temperatures”. *Journal of Physics and Chemistry of Solids* 20 (1-2) 146–149.
- [17] Moreira, T. A., Colmanetti, A. R. A., and Tibiriçá, C. B. (2019). “Heat transfer coefficient: a review of measurement techniques”. *Journal of the Brazilian Society of Mechanical Sciences and Engineering* 41 (6).
- [18] Cullity, B. D. and Graham, C. D. (2008). *Introduction to Magnetic Materials*. 2nd. Wiley.
- [19] Bramwell, S. T. and Harris, M. J. (2020). “The history of spin ice”. *Journal of Physics: Condensed Matter* 32 (37) 374010.
- [20] Kapaklis, V. et al. (2011). “Melting artificial spin ice”. *New Journal of Physics - NEW J PHYS* 14.
- [21] Spaldin, N. (2011). *Magnetic materials : fundamentals and applications*. Cambridge New York: Cambridge University Press.
- [22] COMSOL (n.d.[a]). *What Is Multiphysics?* accessed: 01.6.2021.
- [23] Giraldo, G. (2020). *FEA For Beginners*. accessed: 01.6.2021.
- [24] Zohdi, T. I. (2015). *A Finite Element Primer for Beginners*. Springer International Publishing.
- [25] COMSOL (2017). *The Finite Element Method (FEM)*. accessed: 01.06.2021.
- [26] — (n.d.[b]). *Understanding the Fully Coupled vs. Segregated approach and Direct vs. Iterative linear solvers*. accessed: 09.06.2021.
- [27] Gianfrancesco, A. D. (2017). “Technologies for chemical analyses, microstructural and inspection investigations”. *Materials for Ultra-Supercritical and Advanced Ultra-Supercritical Power Plants*. Elsevier 197–245.
- [28] Lipson, S. G., Lipson, H., and Tannhauser, D. S. (1995). *Optical Physics*. Cambridge University Press.
- [29] Egerton, R. (2016). *Physical Principles of Electron Microscopy*. Springer International Publishing.
- [30] Hopster, H. and H. P. Oepen, eds. (2005). *Magnetic Microscopy of Nanostructures*. Springer Berlin Heidelberg.
- [31] Voigtländer, B. (2019). *Atomic Force Microscopy*. Springer International Publishing.
- [32] Colta, I. (2004). *Lithography in the Nineteenth Century*.
- [33] Thoss, A. (n.d.). *EUV lithography revisited*. <https://www.laserfocusworld.com/blogs/article/14039015/how-does-the-laser-technology-in-euv-lithography-work>. accessed: 11.06.2021.
- [34] Quirk, M. and Serda, J. (2001). *Semiconductor Manufacturing Technology*. Prentice Hall.
- [35] Vinje, J. (2021). “Electron beam lithography: a promising and versatile technique for fabrication of new platforms for cell studies”. PhD thesis. Norwegian University of Science and Technology.
- [36] Cui, Z. (2008). *Nanofabrication*. Springer US.

-
- [37] Parikh, M. (1978). “Self-consistent proximity effect correction technique for resist exposure (SPECTRE)”. *Journal of Vacuum Science and Technology* 15 (3) 931–933.
- [38] Hughes, M. (2016). “What is E-Beam Evaporation?” *Semicore Equipment Inc.*
- [39] Jr, M. C. et al. (2020). “Silicon emissivity as a function of temperature”. *International Journal of Heat and Mass Transfer* 157 119863.
- [40] *ma-N 400 and ma-N 1400 - Negative Tone Photoresists* (2015). ma-N 400 serie. Micro Resist Rechnology GmbH.
- [41] *MEGAPOSITTMSPRTM700 SERIES PHOTORESIST* (2015). SPR700. Rohm and Haas Electronic Materials LLC.
- [42] LaFontaine, W. R., Yost, B., and Li, C.-Y. (1990). “Effect of residual stress and adhesion on the hardness of copper films deposited on silicon”. *Journal of Materials Research* 5 (4) 776–783.
- [43] Xu, M. et al. (2016). “Thermometry of a high temperature high speed micro heater”. *Review of Scientific Instruments* 87 (2) 024904.
- [44] Morley, S. A. et al. (2019). “Thermally and field-driven mobility of emergent magnetic charges in square artificial spin ice”. *Scientific Reports* 9 (1).
- [45] Quero, J. M., Perdignes, F., and Aracil, C. (2018). “11 - Microfabrication technologies used for creating smart devices for industrial applications”. *Smart Sensors and MEMs (Second Edition)*. Ed. by S. Nihtianov and A. Luque. Second Edition. Woodhead Publishing Series in Electronic and Optical Materials. Woodhead Publishing 291–311.
- [46] *MLA150 The Advanced Maskless Aligner* (2019). MLA150. Heidelberg Instruments Mikrotechnik GmbH.
- [47] Vansteenkiste, A. et al. (2014). “The design and verification of MuMax3”. *AIP Advances* 4 (10) 107133.
- [48] Imre, A. (2006). “Majority Logic Gate for Magnetic Quantum-Dot Cellular Automata”. *Science* 311 (5758) 205–208.
- [49] Khojier, K. and Savaloni, H. (2013). “A study on the dependence of DC electrical properties and nanostructure of Cu thin films on film thickness”. *International Journal of Nano Dimension* 3 217–226.
- [50] Smits, F. M. (1958). “Measurement of sheet resistivities with the four-point probe”. *The Bell System Technical Journal* 37 (3) 711–718.
- [51] Beechem, T. et al. (2007). “Invited Article: Simultaneous mapping of temperature and stress in microdevices using micro-Raman spectroscopy”. *Review of Scientific Instruments* 78 (6) 061301.

A | Simulation of micromagnet



(a)



(b)

Figure A.0.1: Two different micromagnetic simulation of a micromagnet of size $2\ \mu\text{m} \times 10\ \mu\text{m}$ using MuMax3. Both simulations stabilised but in **a**) a magnet with several domains was formed and in **b**) a single domain magnet formed. This indicates that it might be possible to form single domain micromagnets.

B | Simulation of single heater

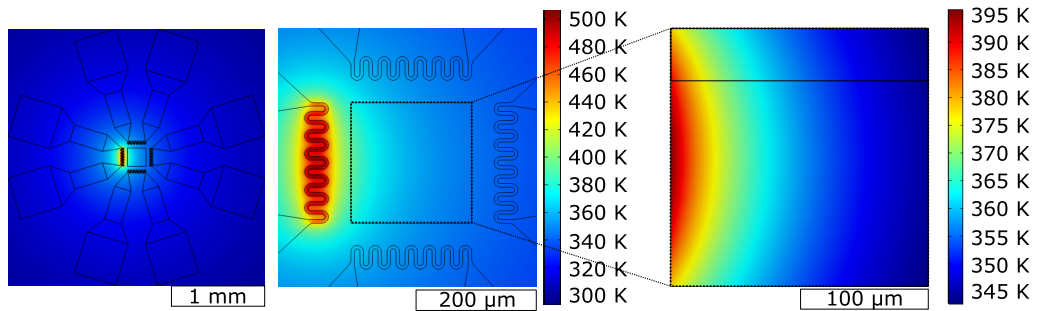


Figure B.0.1: COMSOL Multiphysics simulation of a design where a voltage of 10 V is applied to only one heater. The leftmost figures show the full system at two different scales with the same thermal plot. There is a high temperature of 500 K at the main heating element, but it quickly spreads out towards the edges. The active heating area is shown in the rightmost figure, with a new thermal plot. Here there is a temperature gradient across the area of about 40 K.

